

Phase Structure of Hot and/or Dense QCD with the Schwinger-Dyson Equation

Satoshi TAKAGI^{*)}

Department of Physics, Nagoya University, Nagoya, 464-8602, Japan

We investigate the phase structure of hot and/or dense QCD using the Schwinger-Dyson equation (SDE) with the improved ladder approximation in the Landau gauge. We show that the phase transition from the two-flavor color superconducting (2SC) phase to the quark-gluon plasma (QGP) phase is of second order, and that the scaling properties of the Majorana mass gap and the diquark condensate are consistent with the mean field scaling. We examine the effect of antiquark contribution, and find that setting the antiquark Majorana mass equal to the quark one is a good approximation in the medium density region. We also study the effect of the Debye screening mass of gluon, and find that neglecting of it moves the critical lines to the higher temperature and higher chemical potential region.

§1. Introduction

Dynamics of quantum chromo dynamics (QCD) is very rich and the dynamical chiral symmetry breaking is one of the most important features of QCD. In hot and/or dense matter the chiral symmetry is expected to be restored (see, e.g., Ref. 1), 2)). Furthermore, in recent several years a great interest has been taken in the phenomenon called the “color superconductivity” which occurs after the chiral symmetry restoration at non-zero chemical potential in low temperature region (for a recent review, see, e.g., Ref. 3)). Therefore, the exploration of the QCD phase diagram including the color superconducting phase is an interesting and important subject in view of studying not only the mechanism of the dynamical symmetry breaking but also the phenomenological applications in the cosmology, the astrophysics of neutron stars and the physics of heavy ion collisions.^{3), 1)}

The phase structure of QCD at non-zero temperature with zero chemical potential is extensively studied by the lattice simulation, but the simulations at finite chemical potential have just started and still include large errors [see, e.g., Ref. 4) and references cited therein]. Thus, it is important to investigate the phase structure of QCD in the finite temperature and/or finite chemical potential region by various other approaches.

In various non-perturbative approaches, the approach based on the Schwinger-Dyson Equation (SDE) is one of the most powerful tools [for a review, see, e.g., Refs. 5), 6)]. From the SDE with a suitable running coupling at zero temperature and zero chemical potential, the high energy behavior of the mass function is shown to be consistent with the result derived from QCD by the operator product expansion and the renormalization group equation. When we use the SDE at non-zero

^{*)} E-mail: satoshi@eken.phys.nagoya-u.ac.jp

chemical potential, we can distinguish the Majorana mass of the quark from that of the antiquark by introducing the on-shell projectors of the free quark and the free antiquark, which are useful especially in the high density region where the antiquarks decouple. Furthermore, we can include the effect of the long range force mediated by the magnetic mode of gluon which may give a substantial effect even in the intermediate chemical potential region as in the high density region.^{7),8)} In the SDE analysis, the phase structure of QCD in finite temperature and finite chemical potential region have ever been investigated concentrating on the chiral symmetry restoration.^{9),10),11),12),13),14)} In previous work,¹⁵⁾ by solving the SDE with including full momentum dependences, we studied the phase transition from the hadron phase to the two-flavor color superconducting (2SC) phase in finite quark chemical potential region at zero temperature. It was shown that the phase transition is of first order and the existence of the 2SC phase decrease the critical chemical potential at which the chiral symmetry is restored.

In this paper, we extend the previous work to non-zero temperature and solve the coupled SDE for the Majorana masses of the quark (Δ^-) and antiquark (Δ^+) separately from the SDE for the Dirac mass (B) in the low and intermediate temperature and chemical potential region. The true vacuum is determined by comparing the values of the effective potential at the solutions. In several analyses done so far the SDE with neglecting the antiquark Majorana mass (Δ^+) has been used to estimate the order of the Majorana mass gap at intermediate density ($\mu \sim 300\text{MeV}$).^{8),16),17)} Here we investigate this antiquark effect in the intermediate density region by comparing the results from the SDEs in the following three cases: (case-1) Coupled SDEs for the quark and antiquark Majorana masses; (case-2) SDE for the quark Majorana mass with the antiquark Majorana mass set zero as justified in high density region;^{8),16),17)} (case-3) SDE for the Majorana mass with the antiquark Majorana mass set to be equal to the quark one as used in several analyses done by models with the contact 4-Fermi interaction [see, e.g., Refs. 18),19),20),21),22)]. We solve these three types of SDEs for the Majorana masses and discuss the importance of the antiquark contribution in small chemical potential region. We find that the antiquark mass is same order as the quark one in the low and medium density region ($\mu \lesssim 600\text{MeV}$ where μ is the quark chemical potential) and setting $\Delta^+ = \Delta^-$ is actually a good approximation for investigating the phase diagram, the quark Majorana mass gap and the diquark condensate. Furthermore we investigate the effect of the Debye screening mass of gluon by comparing the results from the SDEs in the case of zero Debye mass with those in the case of non-zero Debye mass. We find that neglectation of the Debye mass of gluon moves the critical lines in the phase diagram to the higher temperature and higher chemical potential region

This paper is organized as follows. In §2, we summarize the quark propagator, the gluon propagator and the running coupling that we use in the present analysis. Several approximations of the quark propagator are made. We also give formulas for calculating the chiral condensate and the diquark condensate. In §3, we present the effective potential for the quark propagator and then derive the Schwinger-Dyson equation as a stationary condition of the effective potential. Section 4 is the main part of this paper, where we give the results of the numerical analysis of

the Schwinger-Dyson equation. Finally, we give a summary and discussion in §5. In the appendices we summarize several intricate expressions and formulas.

§2. Preliminaries

In this section we present the quark propagator, the gluon propagator and the running coupling that we use in the numerical analysis. Using the imaginary time formalism we extend the formalism in Ref. 15) to non-zero temperature [for the quark propagator in the real time formalism, see e.g., Ref. 23)]. Below, p^0 expresses the Matsubara frequency at non-zero temperature T as $p^0 = (2n + 1)\pi iT$. In §2.1, we introduce the eight-component Majorana spinor (Nambu-Gorkov field) and give the general form of the full quark propagator as a matrix in the Nambu-Gorkov space. The gluon propagator with a screening effect is presented in §2.2. We also give the explicit form of the running coupling in the analysis. We give formula to calculate the quark-antiquark condensate and the diquark condensate in §2.3.

2.1. Nambu-Gorkov field and Quark propagator

In the present analysis we regard u and d quarks as massless, but we consider the current mass of the s -quark to be large enough to neglect the strange quark in the formation of the diquark condensate; we assume that the color superconductivity is realized in 2-flavor color superconducting (2SC) phase²⁴⁾ where the color symmetry $SU(3)_c$ is broken down to its subgroup $SU(2)_c$.^{*})

Since we are interested in the phase structure of QCD including the color superconducting phase, it is convenient to use the eight-component Majorana spinor (Nambu-Gorkov field) instead of the four-component Dirac spinor. The Nambu-Gorkov field is expressed as

$$\Psi = \frac{1}{\sqrt{2}} \begin{pmatrix} \psi \\ \psi^C \end{pmatrix}, \quad \psi^C = C\bar{\psi}^T, \quad (2.1)$$

where $C = i\gamma^2\gamma^0$. In the Nambu-Gorkov basis the inverse full quark propagator is expressed as¹⁵⁾

$$iS_F(p)^{-1} = \begin{pmatrix} (p_0 + \mu)\gamma^0 - \vec{\gamma} \cdot \vec{p} - B(p) & \Delta(p) \\ \tilde{\Delta}(p) & (p_0 - \mu)\gamma^0 - \vec{\gamma} \cdot \vec{p} - B(-p) \end{pmatrix}, \quad (2.2)$$

$$\begin{aligned} B(p)_{ij}^{ab} &= B_1(p)\delta^{ij}(\delta^{ab} - \delta^{a3}\delta^{b3}) + B_3(p)\delta^{ij}\delta^{a3}\delta^{b3}, \\ \Delta(p)_{ij}^{ab} &= \epsilon_{ij}\epsilon^{ab3}\gamma_5[\Delta^+(p)A_p^+ + \Delta^-(p)A_p^-], \\ \tilde{\Delta}(p)_{ij}^{ab} &= \gamma^0\Delta(p)_{ij}^{\dagger ab}\gamma^0 \\ &= -\epsilon_{ij}\epsilon^{ab3}\gamma_5[\Delta^+(p)A_p^- + \Delta^-(p)A_p^+], \end{aligned} \quad (2.3)$$

^{*}) We expect that the Color Flavor Locked (CFL) phase²⁵⁾ is realized in the high density region which is out of the region of our analysis, and that the 2SC phase is more stable than the CFL phase near the chiral restoration point.

where i, j and a, b are the flavor and color indices, respectively. We have chosen 3-direction as the direction of color symmetry breaking in such a way that the quarks carrying first two colors make a pair. A_p^- and A_p^+ are the on-shell projectors for the quark and antiquark in the massless limit [for the discussion of massive case, see e.g., Ref. 26)]:

$$A_p^\mp = \frac{1}{2} \left(1 \mp \frac{\gamma^0 \vec{\gamma} \cdot \vec{p}}{\bar{p}} \right). \quad (2.4)$$

Note that in our analysis the chemical potential μ is introduced against the quark number. Now the full quark propagator includes four scalar functions, B_1 and B_3 corresponding to the Dirac masses responsible for the chiral symmetry breaking, while Δ^+ and Δ^- corresponding to the Majorana masses responsible for the color symmetry breaking. As shown in Refs. 11) and 15), the Dirac masses B_1 and B_3 obey the constraint

$$\text{Im} [B_i(p)] = -\text{Im} [B_i(-p)] , \quad (i = 1, 3) \quad (2.5)$$

while, as shown in Ref. 15), the Majorana masses $\Delta^+(p)$ and $\Delta^-(p)$ are real and even functions in p_0 :

$$\Delta^\pm(p) = \Delta^\pm(-p) = [\Delta^\pm(p^*)]^* . \quad (2.6)$$

By taking the inverse of the expression in Eq. (2.2), the full quark propagator is given by

$$-iS_F(p) = \begin{pmatrix} R_+^{-1}(p) & -\{(p_0 + \mu)\gamma^0 - \vec{\gamma} \cdot \vec{p} - B(p)\}^{-1} \Delta(p) R_-^{-1}(p) \\ -\{(p_0 - \mu)\gamma^0 - \vec{\gamma} \cdot \vec{p} - B(-p)\}^{-1} \tilde{\Delta}(p) R_+^{-1}(p) & R_-^{-1}(p) \end{pmatrix}, \quad (2.7)$$

where

$$\begin{aligned} R_+(p) &\equiv \{(p_0 + \mu)\gamma^0 - \vec{\gamma} \cdot \vec{p} - B(p)\} - \Delta(p) \{(p_0 - \mu)\gamma^0 - \vec{\gamma} \cdot \vec{p} - B(-p)\}^{-1} \tilde{\Delta}(p), \\ R_-(p) &\equiv \{(p_0 - \mu)\gamma^0 - \vec{\gamma} \cdot \vec{p} - B(-p)\} - \tilde{\Delta}(p) \{(p_0 + \mu)\gamma^0 - \vec{\gamma} \cdot \vec{p} - B(p)\}^{-1} \Delta(p). \end{aligned} \quad (2.8)$$

2.2. Gluon propagator and Running coupling

In the analyses on the phase structure done before by using the SDE with improved ladder approximation, e.g., in Refs. 9) and 11), the gluon propagator with the same form as that at $T = \mu = 0$ was used. However, in hot and/or dense medium the gluon receives medium effects and effectively becomes massive. In this paper, we include the Debye screening mass of the electric mode of gluon propagator through the hard thermal/dense loop approximation and neglect the Meissner masses, as done in Ref. 15). On the other hand, the form of the magnetic mode used in, e.g., Refs. 7), 8) and 15) can not be extrapolated to zero chemical potential and zero temperature since k_4^2 -term is neglected. In the present analysis, therefore, we drop the Landau damping of the magnetic mode and include the k_4^2 -term.

It should be noticed that the wave function renormalization has to be kept one for the consistency with the bare quark-gluon vertex adopted in the improved ladder approximation.²⁷⁾ At zero temperature and zero chemical potential, we can show that the SDE with the ladder approximation in Landau gauge do not generate the wave function renormalization (see, e.g., Ref. 5)). In the present analysis, therefore, we take the Landau gauge for the gluon propagator with assuming the wave function renormalization for the quark propagator to be one even at non-zero temperature and/or non-zero chemical potential, as was done in Ref. 15).

The explicit form of the gluon propagator that we use in this paper is given by

$$\begin{aligned} D_{\mu\nu}^{AB}(k) &\equiv \delta^{AB} D_{\mu\nu}(k) \\ &= i\delta^{AB} \frac{1}{(k_4)^2 + |\vec{k}|^2} O_{\mu\nu}^{(1)} + i\delta^{AB} \frac{1}{(k_4)^2 + |\vec{k}|^2 + 2M_D^2} O_{\mu\nu}^{(2)}, \end{aligned} \quad (2.9)$$

where $k_4 = -ik_0 = 2\pi nT$ (n : integer) and M_D is the Debye mass of the gluon. In the hard thermal/dense loop approximation the Debye mass is given by²⁸⁾

$$M_D^2 = \alpha_s \left[\frac{\pi}{3} \{2N_c + N_f\} T^2 + \frac{N_f}{\pi} \mu^2 \right], \quad (2.10)$$

where $N_c = N_f = 3$ and the value of α_s is set to be the value at an infrared scale, $\alpha_s(E_f)$ [see Eqs. (2.13)–(2.15)]. $O_{\mu\nu}^{(i)}$ ($i = 1, 2$) are the polarization tensors defined by

$$O_{\mu\nu}^{(1)} = P_{\mu\nu}^\perp + \frac{(u \cdot k)^2}{(u \cdot k)^2 - k^2} P_{\mu\nu}^u, \quad O_{\mu\nu}^{(2)} = -\frac{(u \cdot k)^2}{(u \cdot k)^2 - k^2} P_{\mu\nu}^u, \quad (2.11)$$

where

$$P_{\mu\nu}^\perp = g_{\mu\nu} - \frac{k_\mu k_\nu}{k^2}, \quad P_{\mu\nu}^u = \frac{k_\mu k_\nu}{k^2} - \frac{k_\mu u_\nu + u_\mu k_\nu}{u \cdot k} + \frac{u_\mu u_\nu}{(u \cdot k)^2} k^2. \quad (2.12)$$

The Lorentz four-vector $u^\mu = (1, 0, 0, 0)$ in the gluon propagator reflects the explicit breaking of Lorentz symmetry due to the existence of temperature and/or chemical potential in the rest frame of the medium.

In the improved ladder approximation,²⁹⁾ the high-energy behavior of the running coupling is determined by the one-loop renormalization group equation derived in QCD and the low-energy behavior is suitably regularized. As a result, at zero temperature and zero chemical potential, the high-energy behavior of the mass function derived from the SDE with the running coupling is consistent with that derived from the operator product expansion (OPE).⁵⁾ In the present analysis we use the following two types of running coupling^{29),30),31)} to check the dependences of the results on the methods for the regularization of the infrared behavior:

$$(I) \quad \alpha_s(E) = \frac{g^2(E)}{4\pi} = \frac{12\pi}{11N_c - 2N_f} \cdot f(t, t_f, t_c), \quad (2.13)$$

$$\begin{aligned}
f(t, t_f, t_c) &= \begin{cases} \frac{1}{t} & \text{if } t > t_f, \\ \frac{1}{t_f} + \frac{(t_f - t_c)^2 - (t - t_c)^2}{2t_f^2(t_f - t_c)} & \text{if } t_f > t > t_c, \\ \frac{1}{t_f} + \frac{(t_f - t_c)}{2t_f^2} & \text{if } t_c > t, \end{cases} \\
\text{(II)} \quad \alpha_s(E) &= \frac{g^2(E)}{4\pi} = \frac{12\pi}{11N_c - 2N_f} \cdot \frac{1}{\max(t, t_f)}, \quad (2.14)
\end{aligned}$$

where

$$t = \ln \frac{E^2}{\Lambda_{\text{qcd}}^2}, \quad t_f = \ln \frac{E_f^2}{\Lambda_{\text{qcd}}^2}, \quad t_c = \ln \frac{E_c^2}{\Lambda_{\text{qcd}}^2}, \quad (2.15)$$

with E being the energy scale, Λ_{qcd} the characteristic scale of QCD, and E_f, E_c the infrared cutoff scales introduced to regularize the infrared singularity. Note that the value of the running coupling in the infrared region needs to be sufficiently large in order to involve the dynamical chiral symmetry breaking.²⁹⁾ Here we use the running coupling (I) for $t_f = 0.5$ and $t_c = -2.0$, around which the various physical quantities for $T = \mu = 0$ are very stable with respect to the changes in t_f .³⁰⁾ The running coupling (I) was used in Refs. 9) and 11) while the running coupling (II) was used in the previous work.¹⁵⁾ Therefore, we investigate the dependence of the result on the regularization methods by adopting several values of t_f in both (I) and (II). As discussed in the previous subsection, we assume that the mass of the strange quark is large enough to ignore the s -quark in the formation of the diquark condensate of u and d quarks. On the other hand, it is natural to assume that the current mass of the s -quark is smaller than Λ_{qcd} . In such a case, the effect from the s -quark should be included in the running coupling.^{*)} Thus we set $N_f = 3$ and $N_c = 3$ in the running couplings (2.13) and (2.14).

2.3. Condensates

In this subsection we give formulas to calculate the chiral condensate and the diquark condensate at non-zero temperature. Since we use the imaginary time formalism, the formulas for the condensates are obtained by replacing the integrations over p_4 of the expressions at $T = 0$ in Ref. 15) with the Matsubara sums as $\int \frac{d^4 p}{2\pi} \rightarrow T \sum_n$. In Ref. 15) the logarithmic divergence of the integral is regularized by introducing the ultraviolet (UV) cutoff Λ_4 for the four-dimensional momentum as $-p^2 < \Lambda_4^2$. In the present analysis, on the other hand, we introduce the UV cutoff Λ for the spatial momentum as $|\vec{p}|^2 < \Lambda^2$. Then, the chiral condensate is generally expressed as

$$\langle \Omega | \bar{\psi}_a^i \psi_i^a(0) | \Omega \rangle_\Lambda = -T \sum_n \int^\Lambda \frac{d^3 p}{(2\pi)^3} \text{tr}[S_{F11}], \quad (2.16)$$

where $|\Omega\rangle$ is the state at non-zero temperature and non-zero chemical potential, and the trace is taken in the spinor, flavor and color spaces. Summations over the color index a and the flavor index i are implicitly taken on the left-hand-side

^{*)} As we see later, $\Lambda_{\text{qcd}} \sim 600$ MeV in the present analysis, which is apparently larger than the s -quark mass.

of Eq. (2.16). Similarly to the case of $T = 0$ the formula for the chiral condensate of the charge conjugated quarks is same as that of the quarks shown above:¹⁵⁾ $\langle \Omega | [\bar{\psi}_C]_a^i [\psi_C]_i^a(0) | \Omega \rangle_A = \langle \Omega | \bar{\psi}_a^i \psi_i^a(0) | \Omega \rangle_A$.

The diquark condensate is generally expressed as

$$\langle \Omega | (\epsilon^{ij} \epsilon_{ab3}) [\psi^T]_i^a C \gamma_5 \psi_j^b(0) | \Omega \rangle_A = -T \sum_n \int^A \frac{d^3 p}{(2\pi)^3} \text{tr}[\epsilon^{(c)} \epsilon^{(f)} S_{F12} \gamma_5], \quad (2.17)$$

where $\epsilon^{(c)}$ and $\epsilon^{(f)}$ are antisymmetric matrices in the color and flavor spaces, respectively:

$$\{\epsilon^{(c)}\}^{ab} = \epsilon^{ab3}, \quad \{\epsilon^{(f)}\}_{ij} = \epsilon_{ij}. \quad (2.18)$$

The diquark condensate of the charge conjugated quarks is same as that of the quarks except for the sign:¹⁵⁾ $\langle \Omega | (\epsilon^{ij} \epsilon_{ab3}) [\psi_C^T]_i^a C \gamma_5 [\psi_C]_j^b(0) | \Omega \rangle_A = -\langle \Omega | [\psi^T]_i^a C \gamma_5 \psi_j^b(0) | \Omega \rangle_A$. The explicit forms of the above condensates written in terms of B_i and Δ^\pm are shown in Appendix A.

In the improved ladder approximation at zero temperature and zero chemical potential, the high-energy behavior of the mass function is consistent with that derived from the OPE. The chiral condensate calculated from the mass function was shown to obey the renormalization group evolution derived from the OPE (see, e.g., Refs. 5)). Then, we identify the condensates, which are calculated with UV cutoff Λ , with those renormalized at the scale Λ in QCD. Therefore we scale them to the condensates at 1 GeV using the leading renormalization group formulas. Note that at non-zero temperature the integral over p^0 is converted into the Matsubara sum and the cutoff Λ is introduced for the spatial momentum, not for the four-dimensional momentum as in the Ref. 15). Nevertheless, the relations between the condensates at the scale Λ and those at the scale E are given by the same forms as

$$\langle \Omega | \bar{\psi}_a^i \psi_i^a(0) | \Omega \rangle_E = \left[\frac{\alpha_s(\Lambda)}{\alpha_s(E)} \right]^\kappa \langle \Omega | \bar{\psi}_a^i \psi_i^a(0) | \Omega \rangle_A, \quad (2.19)$$

$$\langle \Omega | (\epsilon^{ij} \epsilon_{ab3}) [\psi^T]_i^a C \psi_j^b(0) | \Omega \rangle_E = \left[\frac{\alpha_s(\Lambda)}{\alpha_s(E)} \right]^{\kappa/2} \langle \Omega | (\epsilon^{ij} \epsilon_{ab3}) [\psi^T]_i^a C \psi_j^b(0) | \Omega \rangle_A, \quad (2.20)$$

where

$$\kappa = \frac{9C_2(F)}{11N_c - 2N_f} = \frac{9}{11N_c - 2N_f} \frac{N_c^2 - 1}{2N_c}. \quad (2.21)$$

§3. Effective potential and the Schwinger-Dyson equation

In this section we present the effective potential for the quark propagator and then derive the Schwinger-Dyson equation (SDE) as a stationary condition of the effective potential.

In the present analysis, we are interested in the differences among the values of the effective potential corresponding to the 2SC vacuum, the chiral symmetry breaking (χ SB) vacuum and the trivial vacuum. Then, as we explained in §2.1, we assume that the current mass of the strange quark is large enough to ignore it in the valence quark sector and we include only u and d quarks in the effective action. In other words, we include the strange quark only as a sea quark in the present analysis. Then, the effective action for the full quark propagator S_F is given by³²⁾

$$\Gamma[S_F] = \frac{1}{2} \left(-i \text{Tr} \text{Ln}(S_F^{-1}) - i \text{Tr}(S_F^{(0)-1} S_F) - i \Gamma_{2\text{PI}}[S_F] \right), \quad (3.1)$$

where Tr and Ln are taken in all the spaces and $\Gamma_{2\text{PI}}[S_F]$ represents the contributions from the two-particle irreducible (with respect to the quark line) diagrams. $S_F^{(0)}$ is the free quark propagator. The factor $1/2$ appears because we use the eight-component Nambu-Gorkov spinor. In high temperature and high density region, the one-gluon exchange approximation is valid since the coupling is weak. In the present analysis, we extrapolate this approximation to intermediate temperature and intermediate chemical potential, and include only the contribution from the one-gluon exchange diagram in $\Gamma_{2\text{PI}}[S_F]$:

$$\Gamma_{2\text{PI}}[S_F] = -\frac{1}{2} \text{Tr}(S_F \cdot ig \Gamma_A^\mu \cdot S_F \cdot ig \Gamma_B^\nu \cdot D_{\mu\nu}^{AB}), \quad (3.2)$$

where Γ_A^μ is the quark-gluon vertex in the Nambu-Gorkov basis defined as

$$\Gamma_A^\mu = \begin{pmatrix} \gamma^\mu T_A & 0 \\ 0 & -\gamma^\mu (T_A)^T \end{pmatrix}. \quad (3.3)$$

From the effective action (3.1), the effective potential in the momentum space is written as

$$\begin{aligned} V[S_F] &= -\Gamma[S_F] / \int d^4x \\ &= \frac{1}{2} \text{T} \sum_n \int \frac{d^3p}{(2\pi)^3} \left(\ln \det\{S_F(p)\} - \text{tr}\{S_F^{(0)-1}(p) S_F(p)\} \right) \\ &\quad + \frac{1}{2} \text{T} \sum_n \int \frac{d^3p}{(2\pi)^3} \text{T} \sum_m \int \frac{d^3q}{(2\pi)^3} \\ &\quad \quad \quad \frac{1}{2} \text{tr}\{S_F(p) \cdot ig \Gamma_A^\mu \cdot S_F(q) \cdot ig \Gamma_B^\nu \cdot i D_{\mu\nu}^{AB}(p-q)\}, \end{aligned} \quad (3.4)$$

where \ln , \det and tr are taken in the spinor, color and flavor spaces.

The SDE is obtained as the stationary condition of the effective potential ($\delta V[S_F]/\delta S_F = 0$):

$$S_F^{-1} = S_F^{(0)-1} - (ig \Gamma_A^\mu \cdot S_F \cdot ig \Gamma_B^\nu) \cdot D_{\mu\nu}^{AB}. \quad (3.5)$$

In this paper we investigate the effect of the antiquark contribution by considering the following three different types of the SDEs: (case-1) SDE with including the quark and antiquark Majorana masses properly; (case-2) SDE with the antiquark Majorana mass neglected as often approximated in the high density region;^{(8), (16), (17)} (case-3) SDE with the quark Majorana mass and the antiquark one set to be equal as in the analyses done by models with the contact 4-Fermi interaction.^{(18), (19), (20), (21), (22)}

case-1

The SDE (3.5) leads to the following four coupled equations for four scalar functions, B_1 , B_3 , Δ^+ and Δ^- :

$$B_1(p) = \text{T} \sum_n \int \frac{d^3q}{(2\pi)^3} \frac{1}{2} \pi \alpha_s D_{\mu\nu}(q-p) \text{tr}[\gamma^\mu T^A S_{F11}(q) \gamma^\nu T^A \delta_1^{(c)}], \quad (3.6)$$

$$B_3(p) = \text{T} \sum_n \int \frac{d^3q}{(2\pi)^3} \pi \alpha_s D_{\mu\nu}(q-p) \text{tr}[\gamma^\mu T^A S_{F11}(q) \gamma^\nu T^A \delta_3^{(c)}], \quad (3.7)$$

$$\Delta^-(p) = \text{T} \sum_n \int \frac{d^3q}{(2\pi)^3} \frac{1}{2} \pi \alpha_s D_{\mu\nu}(q-p) \text{tr}[\gamma^\mu T^A S_{F12}(q) \gamma^\nu (T^A)^T \Lambda_p^- \gamma_5 \epsilon^{(c)} \epsilon^{(f)}], \quad (3.8)$$

$$\Delta^+(p) = \text{T} \sum_n \int \frac{d^3q}{(2\pi)^3} \frac{1}{2} \pi \alpha_s D_{\mu\nu}(q-p) \text{tr}[\gamma^\mu T^A S_{F12}(q) \gamma^\nu (T^A)^T \Lambda_p^+ \gamma_5 \epsilon^{(c)} \epsilon^{(f)}], \quad (3.9)$$

where

$$\{\delta_1^{(c)}\}^{ab} = \delta^{ab} - \delta^{a3} \delta^{b3}, \quad \{\delta_3^{(c)}\}^{ab} = \delta^{a3} \delta^{b3}, \quad (3.10)$$

and the traces are taken in the spinor, flavor and color spaces. The quantity $\alpha_s = \alpha_s(E)$ on the right-hand-sides of Eqs. (3.6)–(3.9) is the running coupling defined in Eqs. (2.13) or (2.14). As was used in Refs. 9), 11) and 15), we use the angular averaged form $E^2 = -p^2 - q^2$ as the argument of the running coupling for $T > 0$ and $\mu > 0$ in the present analysis. The explicit forms of the above coupled equations in Eqs. (3.6)–(3.9) are given in Appendix A. The SDE with distinguishing Δ^- from Δ^+ at non-zero μ is analysed in Refs. 15), 33), where the analyses are done at zero temperature.

case-2

The SDE (3.5) with $\Delta^+ = 0$ leads to the three coupled equations for three scalar functions, B_1 , B_3 and Δ^- : The equation for Δ^- is given by

$$\Delta^-(p) = \text{T} \sum_n \int \frac{d^3q}{(2\pi)^3} \frac{1}{2} \pi \alpha_s D_{\mu\nu}(q-p) \text{tr}[\gamma^\mu T^A S_{F12}^{(\Delta^+=0)}(q) \gamma^\nu (T^A)^T \Lambda_p^- \gamma_5 \epsilon^{(c)} \epsilon^{(f)}]. \quad (3.11)$$

Similarly, the equations for B_1 and B_3 are given by setting $\Delta^+ = 0$ in Eqs. (3.6) and (3.7). The SDE with $\Delta^+ = 0$ is considered to be valid at extremely high density region as used in many works at high density.^{8),16),17)}

case-3

The SDE (3.5) with $\Delta^- = \Delta^+$ leads to the three coupled equations for three scalar functions, B_1 , B_3 and $\Delta^- (= \Delta^+)$: The equation for Δ^- is given by

$$\Delta^-(p) = \text{T} \sum_n \int \frac{d^3q}{(2\pi)^3} \frac{1}{4} \pi \alpha_s D_{\mu\nu}(q-p) \text{tr}[\gamma^\mu T^A S_{F12}^{(\Delta^+=\Delta^-)}(q) \gamma^\nu (T^A)^T \gamma_5 \epsilon^{(c)} \epsilon^{(f)}] . \quad (3.12)$$

The equations for B_1 and B_3 are obtained by setting $\Delta^- = \Delta^+$ in Eqs. (3.6) and (3.7), respectively. This type of the Majorana mass gap is used in several analyses done by the models with the local 4-Fermi interaction^{18),19),20),21),22)} as well as by the SDE.³⁴⁾

As we see in Eq. (2.6), the Majorana masses $\Delta^+(p)$ and $\Delta^-(p)$ are real and even functions in p_0 , while in general the Dirac masses $B_1(p)$ and $B_3(p)$ are complex functions. Equation (2.5) is the constraint on the imaginary part, while no constraint is obtained on the real part from general considerations. However, as shown in Refs. 11) and 15) for the case of $\Delta^+(p) = \Delta^-(p) = 0$, the structure of the SDE leads to a natural constraint on the real parts of the Dirac masses $B_1(p)$ and $B_3(p)$:

$$B_{1,3}(-p) = B_{1,3}^*(p) . \quad (3.13)$$

Using the above properties for B_1 and B_3 and those for Δ^+ and Δ^- in Eq. (2.6), we can always restrict the summation over the Matsubara frequencies to the sum over the positive frequencies.

Substituting the solution of Eq. (3.5) into Eq. (3.4), we obtain the effective potential at the vacuum, i.e., at the stationary point. Since the effective potential itself is divergent, we subtract the effective potential at the trivial vacuum and define

$$\bar{V}_{\text{sol}}[\Delta^+, \Delta^-, B_1, B_3] \equiv V[\Delta^+, \Delta^-, B_1, B_3] - V[0, 0, 0, 0] . \quad (3.14)$$

The value of the effective potential in Eq. (3.14) is understood as the difference between the energy density of the vacuum at the stationary point and that of the trivial vacuum. The true vacuum should be determined by evaluating the value of the effective potential; The vacuum with the smallest value of \bar{V}_{sol} is the most stable vacuum. The explicit form of the above expression is given in Eq. (A.6) in Appendix A.

§4. Numerical analysis

In this section we present the results of the numerical analysis. The only parameter necessary to carry out the numerical analysis is the infrared cutoff parameter t_f in the running coupling. The unit of the energy scale in the numerical analysis is

Λ_{qcd} , and it is determined by calculating the pion decay constant f_π for fixed t_f at zero temperature and zero chemical potential through the Pagels-Stokar formula:³⁵⁾

$$f_\pi^2 = \frac{N_c}{4\pi^2} \int p_E^2 dp_E^2 \frac{B(p) \left(B(p) - \frac{p_E^2}{2} \frac{dB(p)}{dp_E^2} \right)}{[p_E^2 + B^2(p)]^2}. \quad (4.1)$$

We use $f_\pi = 88$ MeV estimated in the chiral limit³⁶⁾ as an input. At zero temperature and zero chemical potential, the dependences of the physical quantities on t_f have been shown to be small around $t_f = 0.5$ for the running coupling (I) with $t_c = -2.0$.³¹⁾ And for the running coupling (II) we checked that the dependences of the physical quantities (mass and condensate) on t_f was small around $t_f = 0.25$. Then, we use $t_f = 0.5$ and $t_c = -2.0$ for the running coupling (I) in Eq. (2.13) and $t_f = 0.25$ for the running coupling (II) in Eq. (2.14) for general T and μ . From these inputs we obtain $\Lambda_{\text{qcd}} = 583$ MeV for the running coupling (I) and $\Lambda_{\text{qcd}} = 567$ MeV for the running coupling (II). Later in this section we will study the dependence of our results on t_f .

We introduce the framework of the numerical analysis in §4.1. In §4.2 we show the phase diagram obtained from the SDE in case-1 and the critical exponents of mass gaps and condensates near the phase transition point from the hadronic phase to the quark-gluon plasma (QGP) phase and that from the 2SC phase to the QGP phase. We investigate the effect of the Debye mass of the gluon in §4.3. In §4.4 we study the effect of the antiquark contribution by solving the coupled SDEs in three cases introduced in the previous section.

4.1. Framework of the numerical analysis

In this subsection we summarize the framework of the numerical analysis. First, as discussed below Eq. (3.13), we restrict the Matsubara sum to the sum over the positive frequency modes using the properties in Eqs. (2.6) and (3.13). Second, to solve the SDEs numerically, we transform the variable $\bar{p} \equiv |\vec{p}|$ into new variable X . For this transformation, we use μ -independent transformation in small chemical potential region ($\mu < \mu_0$) and μ -dependent transformation in medium chemical potential region ($\mu \geq \mu_0$). In small chemical potential region where the chiral condensate is formed, the characteristic scale of the system is Λ_{qcd} . The dynamical information comes mainly from the region $\bar{p} \lesssim \Lambda_{\text{qcd}}$. On the other hand, in the high density region where the diquark condensate is formed, the chemical potential μ , in addition to Λ_{qcd} , gives an important scale. Here, the dynamically important region is $\bar{p} \sim \mu$. Therefore we make the transformation from \bar{p} to X as

$$X = \ln [\bar{p}/\Lambda_{\text{qcd}}] \quad \text{for } \mu < \mu_0, \quad (4.2)$$

$$X = \ln [\bar{p}/(3\mu)] \quad \text{for } \mu \geq \mu_0. \quad (4.3)$$

Here we fix $\mu_0/\Lambda_{\text{qcd}} = 1/3$, since two schemes of the discretization described in Eqs. (4.2) and (4.3) are continuously connected with each other at this point.¹⁵⁾

Under the above transformations, the integration over \bar{p} on the interval $[0, \infty]$ are converted into the integral over X on the interval $[-\infty, \infty]$. In the numerical

integration, we introduce the ultraviolet (UV) and infrared (IR) cutoffs for X , restricting the region as $X \in [\lambda_{IR}, \lambda_{UV}]$. We discretize the interval of X evenly into N_X points:

$$X[J] = \lambda_{IR} + \Delta X \cdot J, \quad J = 0, 1, \dots, N_X - 1, \quad (4.4)$$

where

$$\Delta X = \frac{\lambda_{UV} - \lambda_{IR}}{N_X - 1}. \quad (4.5)$$

The integration over \bar{p} is thus replaced with the following summation:

$$\int d\bar{p} \rightarrow \Delta X \sum_J e^{X[J]}. \quad (4.6)$$

In the present analysis, for the UV and IR cutoffs, we use

$$X : [\lambda_{IR}, \lambda_{UV}] = [-3.5, 2.5]. \quad (4.7)$$

For Matsubara frequency, $p_4 = (2n + 1)\pi T$, we truncate the infinite sum and perform the summation over the $2n_0$ modes labeled by an integer n in the region $n \in [-n_0, n_0 - 1]$. Throughout this paper we use $n_0 = 40$ and $N_X = 40$. We have checked that these values are sufficiently large for the present purpose. To obtain $\langle \bar{\psi}\psi \rangle_{1\text{GeV}}$ and $\langle \psi\psi \rangle_{1\text{GeV}}$, we use Eq. (2.19) and Eq. (2.20) with

$$A = A_{\text{qcd}} \exp(\lambda_{UV}) \quad \text{for } \mu < \mu_0, \quad (4.8)$$

$$A = 3\mu \exp(\lambda_{UV}) \quad \text{for } \mu \geq \mu_0. \quad (4.9)$$

We solve the SDEs in case-1 with an iteration method. Starting from a set of trial functions, we update the mass functions with the SDE:

$$\{B_{1,3\text{old}}, \Delta_{\text{old}}^\pm\} \Rightarrow \boxed{\text{Right-hand sides of SDEs (3.6)-(3.9)}} \Rightarrow \{B_{1,3\text{new}}, \Delta_{\text{new}}^\pm\}. \quad (4.10)$$

Then we stop the iteration when the convergence condition

$$\begin{aligned} \varepsilon A_{\text{qcd}}^6 &> \text{T} \sum_{n=-n_0}^{n_0-1} \int^A \frac{d^3 p}{(2\pi)^3} \frac{1}{4} \text{tr} \left[\left(\frac{\delta V}{\delta[S_F(p)]} \right)^\dagger \left(\frac{\delta V}{\delta[S_F(p)]} \right) \right] \\ &= \text{T} \sum_{n=-n_0}^{n_0-1} \int^A \frac{d^3 p}{(2\pi)^3} \left\{ 2|B_{1\text{old}}(p) - B_{1\text{new}}(p)|^2 + |B_{3\text{old}}(p) - B_{3\text{new}}(p)|^2 \right. \\ &\quad \left. + 2|\Delta_{\text{old}}^+(p) - \Delta_{\text{new}}^+(p)|^2 + 2|\Delta_{\text{old}}^-(p) - \Delta_{\text{new}}^-(p)|^2 \right\} \end{aligned} \quad (4.11)$$

is satisfied with suitably small ε . In the present analysis we set $\varepsilon = 10^{-10}$. In case-2 and case-3, we adopt the same method as that used in case-1.

4.2. Phase Structure

Let us first study the phase structure by solving the SDEs (3·6)–(3·9) in case-1. The resultant phase diagram obtained by using the running coupling of type (I) with $t_f = 0.5$ and $M_D \neq 0$ is shown in Fig. 1. In the present analysis we consider the possibility of three phases; the hadron (χ SB) phase, the 2SC phase and the QGP phase. We determine the true vacuum by evaluating the value of the effective potential at the solution of the SDE. The running coupling of type (I) in Eq. (2·13) used here becomes very large in the infrared region. It exceeds the critical value $\pi/2$,^{*)} above which the SDE for the Majorana mass with zero Dirac mass ($B = 0$) provides the non-trivial solution even at $T = \mu = 0$. Then, similarly to what we have shown for $\mu > 0$ and $T = 0$ in Ref. 15), even for non-zero but small temperature, there always exists the 2SC vacuum where the non-trivial Majorana mass is dynamically generated, and the 2SC vacuum is more stable than the trivial

^{*)} At $T = \mu = 0$, the SDE for $\Delta = \Delta^- = \Delta^+$ takes the same form as that for the Dirac mass B except that an extra factor of 1/2 appears in front of the integration kernel. Since the critical value of the coupling in the SDE for B is $\pi/4$,⁵⁾ the extra factor of 1/2 implies that the critical value of the coupling in the SDE for Δ is $\pi/2$.

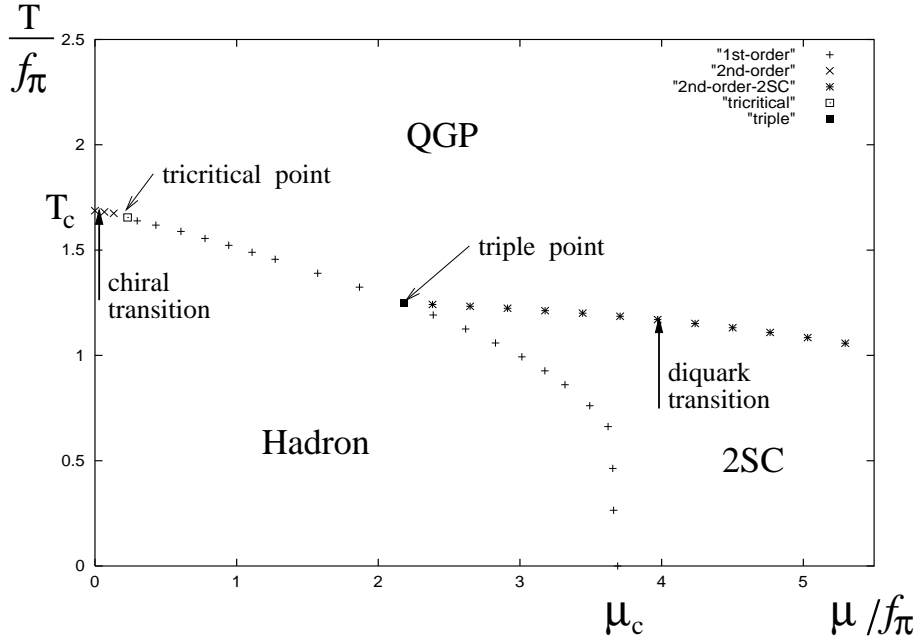


Fig. 1. Phase diagram for $0 \leq T/f_\pi \leq 2.5$ and $0 \leq \mu/f_\pi \leq 5.5$. The symbol \times denotes the second order phase transition point between the hadron phase and the QGP phase, $+$ the first order phase transition point between the hadron phase and the QGP phase or the 2SC phase. The symbol $*$ denotes the second order phase transition point between the 2SC phase and the QGP phase. $T_c=147$ MeV, $\mu_c=325$ MeV, and $(T, \mu)=(146, 20)$ MeV at the tricritical point where the second order phase transition changes into the first order. At the “triple point”, $(T, \mu)=(110, 192)$ MeV where hadron phase ($\langle \bar{\psi}\psi \rangle \neq 0$), 2SC phase ($\langle \psi\psi \rangle \neq 0$) and QGP phase ($\langle \bar{\psi}\psi \rangle = \langle \psi\psi \rangle = 0$) meet together.

vacuum (QGP vacuum in the present analysis). In the low chemical potential region, there also exists the χ SB vacuum where the Dirac mass B is dynamically generated, and it is most stable among three vacua. Hence the true vacuum in low temperature and low chemical potential region is the χ SB vacuum. This is natural because the strength of the attractive force mediated by one-gluon exchange between two quarks in the color antitriplet channel is weaker than that between a quark and an antiquark in the color singlet channel at $T = \mu = 0$. When the temperature is increased at $\mu = 0$, the value of the effective potential at the 2SC vacuum goes to zero smoothly around $T \sim 110$ MeV ($T/f_\pi \sim 1.3$), while the χ SB vacuum is still the most stable. Up until this region, the chiral condensate $\langle \bar{\psi}\psi \rangle$ does not change its value so much as we show in Fig. 2. As the temperature is increased further, the chiral condensate

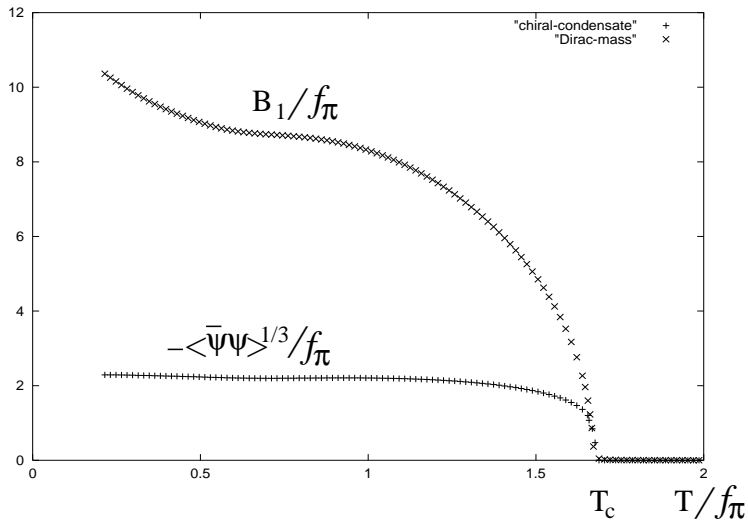


Fig. 2. Temperature dependences of the chiral condensate and the Dirac mass gap at $\mu = 0$. Here the critical temperature of the chiral phase transition from the hadron phase to the QGP phase at $\mu = 0$ is $T_c = 147$ MeV.

starts to decrease, and it as well as the mass function at zero-momentum limit (shown by B_1/f_π in Fig. 2) finally goes to zero at $T/f_\pi = 1.67$, i.e.,

$$T_c = 147 \text{ MeV} \quad (\mu = 0) . \quad (4.12)$$

At the same time, the value of the effective potential at χ SB vacuum is also smoothly going to zero, i.e., the value of the trivial vacuum. Then, at $\mu = 0$ the phase transition occurs from the hadron phase to the QGP phase (the chiral phase transition), and it is of second order. This is consistent with previous analyses done by the SDE (see, e.g., Refs. 12), 9), 11), 13), 37)).

We obtain the tricritical point at

$$(T_t, \mu_t) = (146, 20) \text{ MeV} , \quad (4.13)$$

(indicated by \square in Fig. 1): For $\mu > \mu_t$ the chiral phase transition is of first order (indicated by $+$ in Fig. 1), while for $\mu < \mu_t$ it is of second order (indicated by \times in

Fig. 1). The value of the chemical potential at the tricritical point obtained in the present analysis is smaller than those in several other models such as the instanton model,¹⁸⁾ the NJL model^{20),21)} and the random matrix model²²⁾ as well as in the analysis done by the SDE^{12),13)} but is consistent with that obtained in Ref. 11) analyzed by the SDE. We find that in the framework of the SDE the large difference of the position of the tricritical point on T- μ plane is caused by the existence of the imaginary part of the Dirac mass. We will discuss this point in §5.

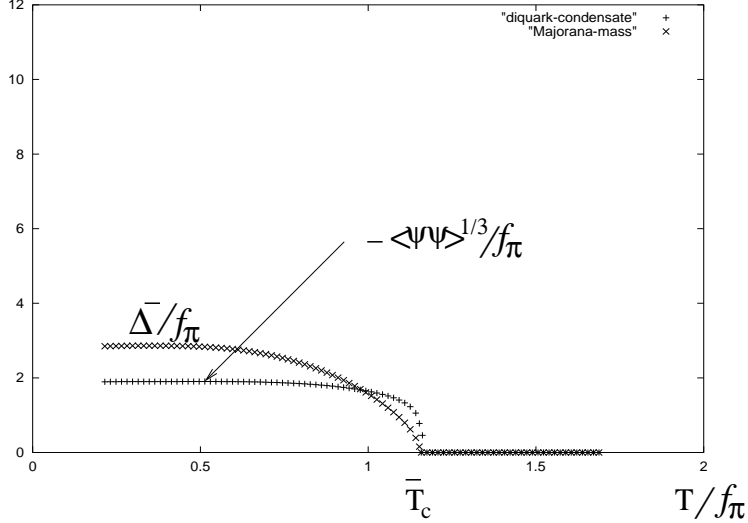


Fig. 3. Temperature dependences of the diquark condensate and the Majorana mass gap at $\mu/f_\pi = 4$. Here, the critical temperature of the color phase transition from the 2SC phase to the QGP phase at $\mu/f_\pi = 4$ is $\bar{T}_c = 102$ MeV.

When we increase the chemical potential at $T = 0$, on the other hand, the 2SC vacuum overcomes the χ SB vacuum at the critical chemical potential $\mu/f_\pi = 3.69$, i.e.,

$$\mu_c = 325 \text{ MeV} \quad (T = 0) , \quad (4.14)$$

before the χ SB vacuum becomes less stable than the trivial vacuum. As a result the phase transition occurs from the hadron phase to the 2SC phase, and it is of first order. This structure is same as that obtained in Ref. 15) where the form of the gluon propagator was different from the present one in Eq. (2.9) and the running coupling of type (II) in Eq. (2.14) was used. Let us increase the temperature in the 2SC phase. The temperature dependences of the diquark condensate $\langle\psi\psi\rangle$ and the Majorana mass gap of quark Δ^- for $\mu/f_\pi = 4$ are shown in Fig. 3. This shows that the diquark condensate and the Majorana mass gap are stable against the change of the temperature in the low temperature region ($T/f_\pi \lesssim 0.6$, i.e., $T \lesssim 50$ MeV). Around $T \sim 50$ MeV the condensate and the mass gap start to decrease and they go to zero at $T = \bar{T}_c = 1.15f_\pi = 102$ MeV. At the same time, the value of the effective potential at the 2SC vacuum smoothly vanishes. Then, the phase transition from the 2SC phase to the QGP phase occurs, and this color phase transition is of

second order. This is consistent with the result obtained in the models with 4-Fermi interaction.^{18),21)} However, as we can see from Fig. 1, the critical temperature of the color phase transition obtained in the present analysis is around 100 MeV for any μ of $\mu \lesssim 500$ MeV, and this value is larger than the values obtained in the models based on the contact 4-Fermi interaction.^{18),20),21)} This enlargement of the critical temperature may be caused by the long range force mediated by the magnetic mode of the gluon. We will be back to this point in the next subsection.

Let us consider the critical behaviors of the condensates and the mass gaps near the second order phase transition points along the arrows labeled by ‘‘chiral transition’’ ($\mu = 0$) and ‘‘diquark transition’’ ($\mu/f_\pi = 4$) shown in Fig. 1. First we consider the chiral second order phase transition at zero chemical potential. In Refs. 38), 13), 14), 37), it was shown that, by using SDEs with different kernels, the scaling properties of the chiral condensate and the Dirac mass gap near the critical temperature are consistent with those of the mean field. Furthermore, the previous analyses done in Refs. 9), 37) by the SDE with similar kernel concluded that the scaling is consistent with the mean field one, although the numerical errors are not clear. Thus, in the present analysis, we assume the mean field scaling of the condensate and the mass gap, and fit the values of the prefactor and the critical temperature by minimizing

$$\sum_i |y(\mathbf{T}_i) - F(\mathbf{T}_i, k)|^2, \quad (4-15)$$

where index i labels the temperature, y is the chiral condensate $-\langle\bar{\psi}\psi\rangle$ or the Dirac mass gap at infrared limit $B_1(p_0 = \bar{p} = 0)$, and $F(\mathbf{T}, k)$ is the fitting function given by

$$F(\mathbf{T}, k) = k \left(1 - \frac{\mathbf{T}}{\mathbf{T}_c}\right)^{1/2}. \quad (4-16)$$

Performing the fit for $0.9\mathbf{T}_c \lesssim \mathbf{T} < \mathbf{T}_c$, we obtain the following best fitted values for the prefactor and the critical temperature:

$$-\langle\bar{\psi}\psi\rangle \sim a \left(1 - \frac{\mathbf{T}}{\mathbf{T}_c}\right)^{1/2}, \quad a \sim 37.3 f_\pi^3, \quad \mathbf{T}_c \sim 147 \text{ [MeV]}, \quad (4-17)$$

$$B_1(p_0 = \bar{p} = 0) \sim \alpha \left(1 - \frac{\mathbf{T}}{\mathbf{T}_c}\right)^{1/2}, \quad \alpha \sim 15.9 f_\pi, \quad \mathbf{T}_c \sim 147 \text{ [MeV]}. \quad (4-18)$$

We show the fitting function in Eq. (4-16) with the above best fitted values in the left panel of Fig. 4 together with the numerical data obtained from the solution of the SDE. This figure shows that the critical behaviors of the chiral condensate $-\langle\bar{\psi}\psi\rangle$ and the Dirac mass gap $B_1(p_0 = \bar{p} = 0)$ near $\mu = 0$ are consistent with the mean field scaling.

We next consider the critical behaviors of the diquark condensate $\langle\psi\psi\rangle$ and the Majorana mass gap on the Fermi surface $\Delta^-(p_0 = 0, \bar{p} = \mu)$ near the color second order phase transition at $\mu/f_\pi = 4$ along the arrow labeled by ‘‘diquark transition’’ in Fig. 1. Using the same fitting method as used above for the chiral transition, we

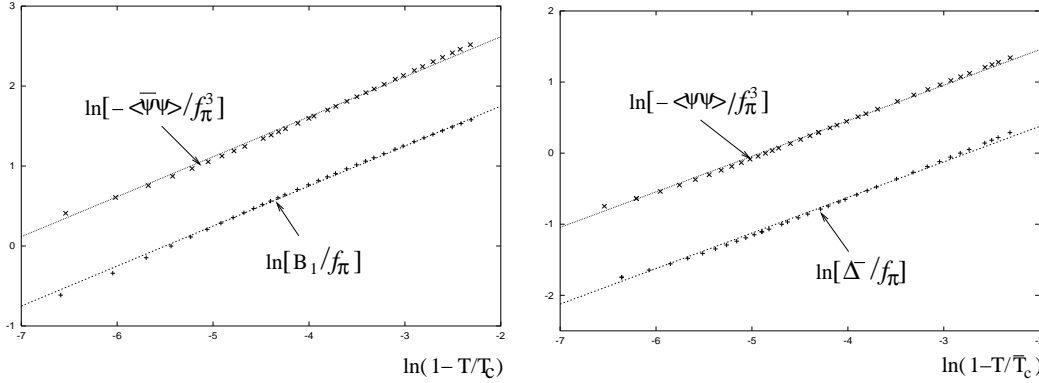


Fig. 4. Critical behaviors of the condensates and the mass gaps. The left panel shows the critical behaviors of the chiral condensate $-\langle\bar{\psi}\psi\rangle$ and the Dirac mass gap $B_1(p_0 = \bar{p} = 0)$ near the chiral second order phase transition at $\mu/f_\pi = 0$ along the arrow labeled by “chiral transition” in Fig. 1. While the right panel shows those of the diquark condensate $-\langle\psi\psi\rangle$ and the Majorana mass gap $\Delta^-(p_0 = 0, \bar{p} = \mu)$ near the diquark second order phase transition at $\mu/f_\pi = 4$ along the arrow labeled by “diquark transition” in Fig. 1. Solid lines in the left panel show the fitting functions shown in Eqs. (4-17) and (4-18), and those in the right panel the fitting functions in Eqs. (4-19) and (4-20).

perform the fit for $0.9\bar{T}_c \lesssim T < \bar{T}_c$. The best fitted values of the critical temperature and the prefactor are determined as

$$-\langle\psi\psi\rangle \sim \bar{a} \left(1 - \frac{T}{\bar{T}_c}\right)^{1/2}, \quad \bar{a} \sim 11.6 f_\pi^3, \quad \bar{T}_c \sim 102 \text{ [MeV]}, \quad (4-19)$$

$$\Delta^-(p_0 = 0, \bar{p} = \mu) \sim \bar{\alpha} \left(1 - \frac{T}{\bar{T}_c}\right)^{1/2}, \quad \bar{\alpha} \sim 3.9 f_\pi, \quad \bar{T}_c \sim 102 \text{ [MeV]}. \quad (4-20)$$

We show the resultant fitting functions together with the numerical results in the right panel of Fig. 4. This shows that the critical behaviors near the diquark phase transition point are consistent with the mean field scaling.

4.3. Effect of the Debye mass of gluon

In this subsection we study the influence of the Debye mass of gluon on the phase diagram in case-1. In Fig. 5 we show the change of the phase diagram due to the Debye mass. This shows that neglecting the Debye mass does not change the following qualitative structure of the phase diagram: There is a tricritical point which divides the critical line for the chiral phase transition from the hadron phase to the QGP phase into the critical line for the second order transition and the one for the first order transition; The phase transition from the hadron phase to the 2SC phase is of first order, while the color phase transition from the 2SC phase to the QGP phase is of second order. However, the effect of the Debye mass changes the quantitative structure. In the case of zero Debye mass the phase diagram without including the 2SC phase is same as that in Ref. 11). When we include the 2SC phase to draw the phase diagram, the critical chemical potential becomes smaller than that in Ref 11): At $T = 0$, $\mu_c = 460 \text{ MeV}$ is obtained in Ref 11), while we

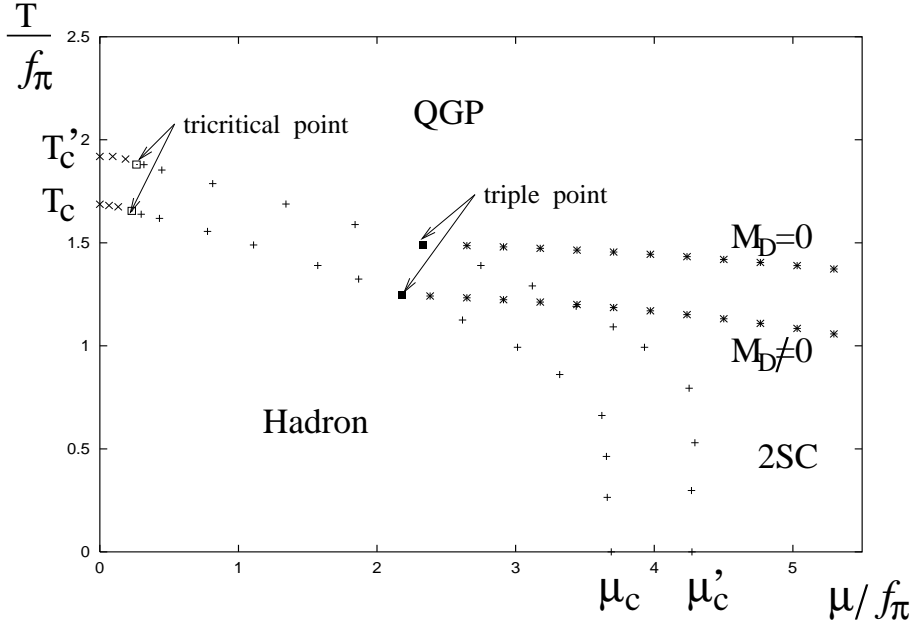


Fig. 5. Phase diagram for $0 \leq T/f_\pi \leq 2.5$ and $0 \leq \mu/f_\pi \leq 5.5$ obtained by setting $M_D = 0$ in the SDE. For comparison, the phase diagram shown in Fig. 1 obtained with including the Debye mass is also drawn. Here $T_c=147$ MeV, $\mu_c=325$ MeV, $T'_c=169$ MeV and $\mu'_c=376$ MeV.

obtain $\mu_c = 376$ MeV. This is further reduced to $\mu_c = 325$ MeV by including the Debye screening mass into the electric mode of the gluon. Similarly, the critical line dividing the hadron phase from the 2SC phase is moved to smaller chemical potential region by about 15% when the Debye mass is included. Furthermore, the inclusion of the Debye mass lowers the value of the critical temperature at the phase transition from the hadron phase to the QGP phase by about 15% while the value of the critical temperature at the phase transition from the 2SC phase to the QGP phase by 15~30%. Note, however, that the value of the chemical potential at the tricritical point is not changed although the value of the critical temperature at the point decreases by about 15%. These quantitative changes imply that the Debye mass of the electric mode plays a role to weaken the attractive interaction between two quarks as well as that between a quark and an antiquark. This is reasonable because the Debye mass screens the long range force mediated by the electric mode of gluon. Therefore we expect that the critical temperatures of the chiral and color phase transition from the hadron phase and the 2SC phase to the QGP phase may be further reduced if the contact interaction, i.e., the short-range force induced by the instanton, is a dominant one in this intermediate chemical potential region.

4.4. Effect of antiquark contribution

In this subsection we study the effect of the antiquark contribution by solving the following three different types of SDEs: (case-1) Coupled SDEs for Δ^- and Δ^+ ; (case-2) SDE for Δ^- with $\Delta^+ = 0$; (case-3) SDE for Δ^- with $\Delta^+ = \Delta^-$. In case-1 the quark mass and the antiquark mass are included properly while the antiquark

mass is neglected completely in case-2. The approximation in case-2 is considered to be valid in the high density region. On the other hand, the approximation in case-3 is used in many analyses done by the models with the local 4-Fermi interaction.

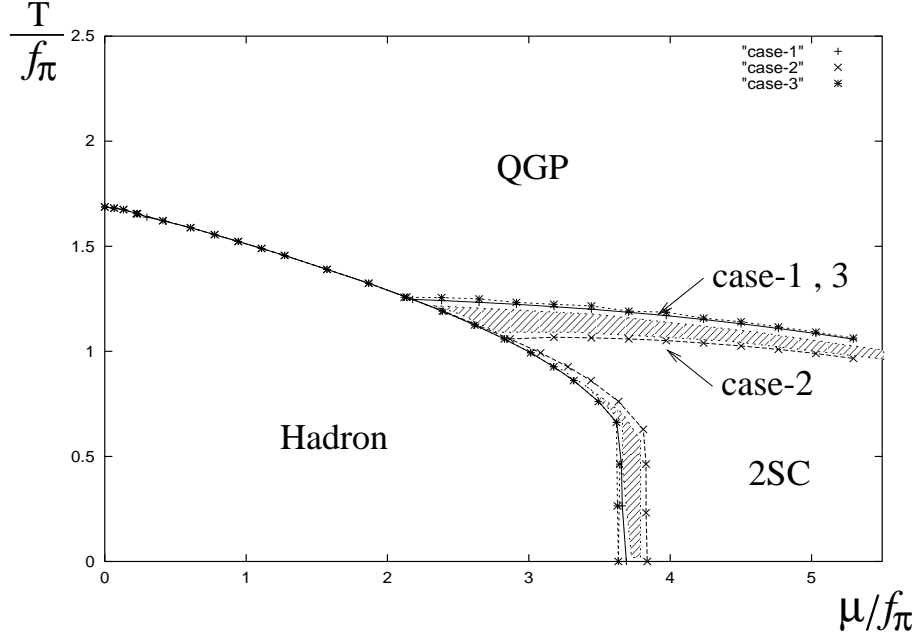


Fig. 6. Phase diagrams for three different cases for $0 \leq T/f_\pi \leq 2.5$ and $0 \leq \mu/f_\pi \leq 5.5$. The symbol $+$ denotes the phase transition point in case-1, \times that in case-2 and $*$ that in case-3. The points in case-1 are connected by solid lines, and those in case-2 and case-3 are by dashed lines and dotted lines, respectively. The shaded areas are in the 2SC phase in case-1 but not in case-2.

We show the phase diagrams of above three different cases in Fig. 6. In this figure the symbol $+$ denotes the phase transition point in case-1, \times that in case-2 and $*$ that in case-3. To make the differences among three cases clearly, we connect the data points by solid line in case-1, by dashed line in case-2 and by dotted line in case-3. First of all, we should note that the critical line between the hadron phase and the QGP phase for $\mu/f_\pi \lesssim 2$ is not at all affected by the change of the antiquark contribution since there do not exist the 2SC solutions. Then, in all three cases, we obtained the same tricritical point at $(T, \mu) = (146, 20)$ MeV where the critical line is divided into the line for the second order phase transition ($\mu < 20$ MeV) and the one for the first order phase transition ($20 \text{ MeV} < \mu \lesssim 180$ MeV). Similarly to the effect of Debye mass studied in the previous subsection, the effect of antiquark contribution does not change the following qualitative structures of the phase diagram: In all three cases, the phase transition from the hadron phase to the 2SC phase is of first order, while the color phase transition from the 2SC phase to the QGP phase is of second order. Furthermore, the approximation of $\Delta^+ = \Delta^-$ (case-3) provides almost the same phase diagram as for the full analysis (case-1) except that the critical chemical potential at $T \simeq 0$ in case-3 is slightly smaller than that in case-1. However, the

neglection of the antiquark contribution (case-2) quantitatively changes the critical line between the hadron phase and the 2SC phase as well as that between the 2SC phase and the QGP phase. In Fig. 6, we show the region in the 2SC phase in case-1 but not in case-2 by the shaded areas. This clearly shows that the region of 2SC phase in case-2 is smaller than that in case-1 as well as in case-3. The value of the critical temperature at the color phase transition in case-1 becomes larger about 10% at $\mu/f_\pi = 4$ than that in case-2. The value of the critical chemical potential at the chiral phase transition in case-1 becomes smaller about 5% at zero temperature than that in case-2.

Let us study the Majorana mass gap and the diquark condensate at zero temperature. In the remainder of this subsection, we study them not only at the true vacuum (i.e., the 2SC vacuum is the most stable) but also at the false vacuum (i.e., the 2SC vacuum is less stable than the χ SB vacuum) in order to see the effect of antiquark contribution more clearly.

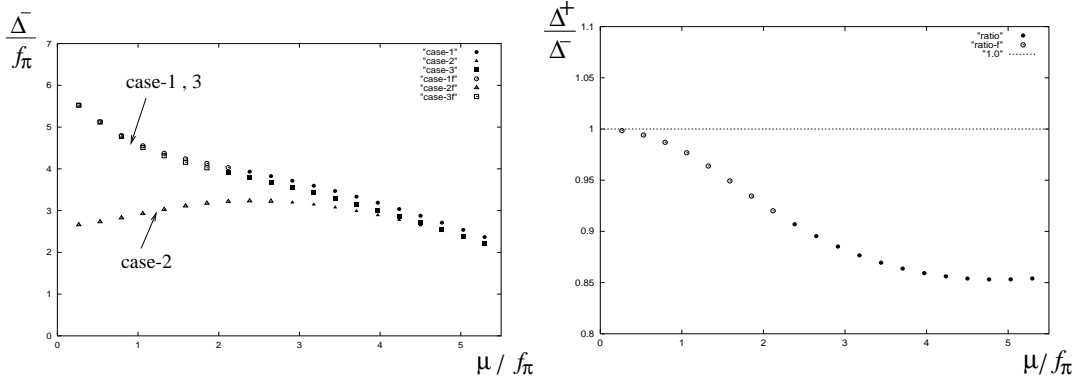


Fig. 7. Chemical potential dependences of the $\Delta^-(p_0 = 0, \bar{p} = \mu)$ in three cases (left panel) and $\Delta^+(p_0 = 0, \bar{p} = \mu)/\Delta^-(p_0 = 0, \bar{p} = \mu)$ in case-1 (right panel) for $0 \leq \mu/f_\pi \leq 5.5$ and $T = 0$. In the left panel, the data points indicated by circle, triangle and square are obtained in case-1, case-2 and case-3, respectively. The blank symbols (\circ , \triangle and \square) imply the data points in the false vacuum (the 2SC vacuum is less stable than the χ SB vacuum), while the filled ones in the true vacuum (the 2SC vacuum is most stable).

In Fig. 7 we show the chemical potential dependences of the quark Majorana mass gap Δ^- on the Fermi surface (left panel) and the ratio of the antiquark mass to the quark one Δ^+/Δ^- at $p_0 = 0$ and $\bar{p} = \mu$ in case-1 (right panel) at zero temperature. We should note that a nontrivial solution exists in all the cases even at $\mu = 0$ since the running coupling in the infrared region exceeds the critical value $\pi/2$ as we have discussed in subsection 4.2. Furthermore, the ratio Δ^+/Δ^- is actually one at $\mu = 0$, which is required by the existence of the charge conjugation symmetry. As a result, Δ^- in case-3 exactly agrees with that in case-1 at $\mu = 0$. On the other hand, the value of Δ^- in case-2 is about half of those in case-1 and case-3 at $\mu = 0$. When we increase the chemical potential, the values of Δ^- in case-1 and case-3 decrease, while that in case-2 once increases and then decreases. The right panel of Fig. 7 shows that the ratio Δ^+/Δ^- in case-1 decreases with μ and reach about 0.85. The left panel of Fig. 7 shows that, for $\mu/f_\pi \gtrsim 3.5$, the values of Δ^-

in all three cases are almost same although the values of Δ^+ have large difference; $\Delta^+(\text{case-1}) : \Delta^+(\text{case-2}) : \Delta^+(\text{case-3}) \simeq 0.85 : 0 : 1$. These results imply that the antiquark gives a sizable contribution to the quark Majorana mass in the low chemical potential region while it becomes negligible for $\mu/f_\pi \gtrsim 3.5$. This may indicate that, to form the Majorana mass in the region where the 2SC vacuum is actually most stable, the effect of Fermi surface is more important than the effect of large attractive force due to the large running coupling.

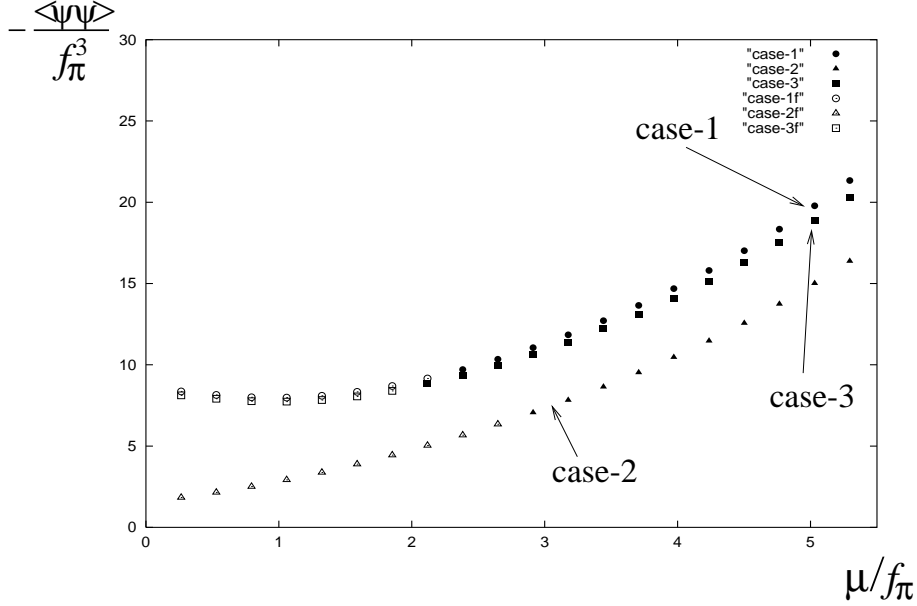


Fig. 8. Chemical potential dependences of the diquark condensates for $0 \leq \mu/f_\pi \leq 5.5$ and $T = 0$. The data points indicated by circle, triangle and square are obtained in case-1, case-2 and case-3, respectively. The blank symbols (\circ , \triangle and \square) imply that the data points are in the false vacuum (the 2SC vacuum is less stable than the χ SB vacuum), while the filled ones in the true vacuum (the 2SC vacuum is most stable).

Next, we show the chemical potential dependences of the diquark condensates in three cases in Fig. 8. This shows that the value of the diquark condensate in case-3 ($\Delta^+ = \Delta^-$) is almost same as that in case-1, which is consistent with the fact that in case-1 the value of Δ^+ is comparable with that of Δ^- . On the other hand, there is a large difference between the value of the diquark condensate in case-2 and that obtained in case-1. Actually, the ratio of the value of the diquark condensate in case-1 or case-3 to that in case-2 is roughly four in the very low chemical potential region: $\langle \psi\psi \rangle_{\text{case-1}} / \langle \psi\psi \rangle_{\text{case-2}} \simeq 4$ for $\mu \simeq 0$. This can be understood as follows: Figure 7 shows that the value of Δ^- in case-1 is about double of that in case-2 for $\mu \simeq 0$, and that Δ^+ is comparable to Δ^- in case-1 for $\mu \simeq 0$. On the other hand, the formula for calculating the diquark condensate in Eq. (A.5) shows that the diquark condensate consists of the quark and antiquark contributions, and that the dominant part comes from the ultraviolet region. Thus, each of quark and antiquark contributions to the diquark condensate in case-1 is about twice of the quark contribution in case-2 and

then the ratio of the value of the diquark condensate in case-1 or case-3 to that in case-2 is about four near $\mu = 0$. Now, how about the ratio in the intermediate chemical potential region ($\mu/f_\pi \gtrsim 3.5$)? If the effect of the Fermi surface were negligible, the same argument as above would lead us to conclude that the values of diquark condensate in case-3 and case-1 are roughly twice of that in case-2. However, Fig. 8 shows that the ratio is actually smaller than two and it becomes about 4/3 at $\mu/f_\pi = 5$: $\langle\psi\psi\rangle_{\text{case-1}}/\langle\psi\psi\rangle_{\text{case-2}} \simeq 4/3$ for $\mu/f_\pi = 5$. This implies that, as is expected, the effect of the Fermi surface plays an important role in the intermediate chemical potential region.

The results we have shown in this subsection so far (Figs. 6, 7 and 8) imply that the antiquark gives a non-negligible contribution, and that the approximation $\Delta^- = \Delta^+$ is sufficient to study the phase diagram, the quark Majorana mass gap and the diquark condensate in intermediate temperature and intermediate chemical potential region where the chiral phase transition occurs. Presumably, the same approximation may be enough to investigate other physical quantities such as the number density.

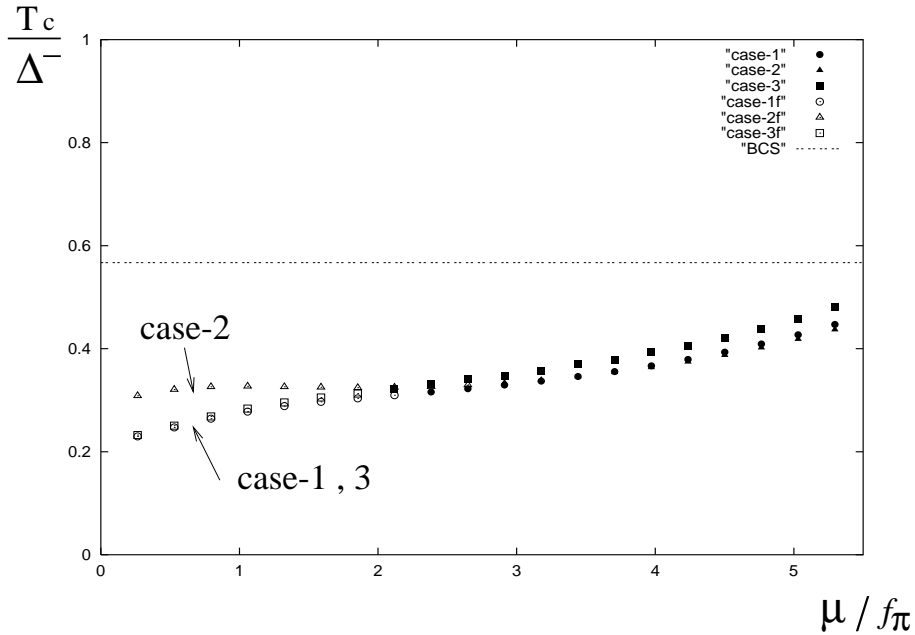


Fig. 9. Chemical potential dependences of the ratios of T_c to $\Delta^-(p_4 = 0; \bar{p} = \mu)|_{T=0}$ for $0 \leq \mu/f_\pi \leq 5.5$. The data points indicated by circle, triangle and square are obtained in case-1, case-2 and case-3, respectively. The blank symbols (\circ , \triangle and \square) imply that the data points are in the false vacuum (the 2SC vacuum is less stable than the χ SB vacuum), while the filled ones in the true vacuum (the 2SC vacuum is most stable).

Let us compare the results of the ratio of the critical temperature to the Majorana mass gap at zero temperature with the BCS result, $T_c/\Delta \simeq 0.567$, obtained in the high density region.^{17),39)} In Fig. 9 we show the chemical potential dependences of the ratios of the critical temperature to the quark Majorana mass gap on the

Fermi surface at zero temperature. There are only small differences among the data points obtained in three cases. From this figure we see that this ratio approaches the BCS value 0.567 when we increase the value of the chemical potential, and that it is already close enough in the intermediate chemical potential region:

$$T_c/\Delta^- \sim 0.5, \quad \text{for } \mu \sim 450 \text{ MeV}. \quad (4-21)$$

Finally, we check the model dependence of the phase diagram by changing the infrared regularization parameters in two types of running couplings in Eqs. (2-13) and (2-14). We show the phase diagrams for the running coupling of type (I) with $t_f = 0.4, 0.5$ and 0.6 in the left panel of Fig. 10 and the phase diagrams for the running coupling of type (II) with $t_f = 0.20, 0.25$ and 0.30 in the right panel of Fig. 10. These figures show that the critical line for the phase transition from

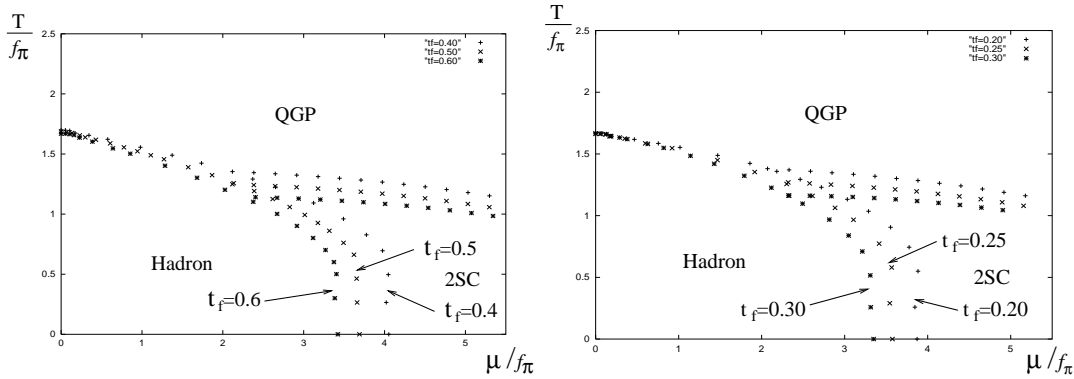


Fig. 10. Phase diagram for several choices of the infrared cutoff parameter t_f . Left panel shows the critical lines for $t_f = 0.4, 0.5$ and 0.6 in the running coupling of type (I) in Eq. (2-13). Right panel shows the critical lines for $t_f = 0.2, 0.25$ and 0.3 in the running coupling of type (II) in Eq. (2-14).

the hadron phase to the 2SC phase as well as that from the 2SC phase to the QGP phase has a small dependence on the infrared regularization parameter t_f : For larger value of t_f , the phase transition from the hadron phase to the 2SC phase occurs at the smaller chemical potential, and that from the 2SC phase to the QGP phase at the smaller temperature. On the other hand, the critical line for the chiral phase transition from the hadron phase to the QGP phase is very stable against the change of t_f in both types of the running coupling. Furthermore, the running coupling of type (II) with $t_f = 0.25$ gives almost the same critical line for the chiral phase transition as the type (I) with $t_f = 0.5$ gives. These imply that the phase structure in the small chemical potential region is very insensitive to the infrared regularization of the running coupling.

§5. Summary and Discussion

We studied the phase structure of hot and/or dense QCD by solving the Schwinger-Dyson equations for the Dirac and Majorana masses of the quark propagator with

the improved ladder approximation in the Landau gauge. We found that there exists a tricritical point at $(T, \mu) = (146, 20)$ MeV which divides the critical line between the hadron phase and the QGP phase into the line of second order phase transition (in between $(T, \mu) = (147, 0)$ MeV and $(146, 20)$ MeV) and the one of first order phase transition ($20 \text{ MeV} < \mu$). Our result implies that, at the second order phase transition at $\mu = 0$, the scaling properties of the Dirac mass and the chiral condensate are consistent with the mean field scalings.

The phase transition from the hadron phase to the 2SC phase was found to be of first order at non-zero temperature as we have obtained at zero temperature in the previous analysis.¹⁵⁾ Furthermore, we found that the color phase transition from the 2SC phase to the QGP phase is of second order with the scaling properties of the Majorana mass and the diquark condensate consistent with the mean field scalings. The resultant critical temperature of the color phase transition is on the order of 100 MeV which is about double of the value obtained in the analyses done by the models based on the contact 4-Fermi interaction (see, e.g., Refs. 18), 20), 21)). We think that this enlargement of the critical temperature may be caused by the long range force mediated by the magnetic mode of the gluon.

In the present paper we performed the analysis with including the imaginary part of the Dirac mass, because in the SDE at non-zero chemical potential, the imaginary part, which is momentum dependent (odd function in p_0), is inevitably generated in the hadron (χSB) phase. However some analyses of the SDE do not include the imaginary part and the analyses done by the local 4-Fermi interaction model do not generally include the imaginary part because the leading order approximation is used there. We found that the most remarkable feature of the inclusion of the imaginary part of the Dirac mass is in the position of the tricritical point on T - μ plane. When we use the SDE with neglecting the imaginary part of the Dirac mass i.e., $\text{Im}[B(p)] = 0$, the tricritical point is at $(T, \mu) = (124, 210)$ MeV (The triple point is at $(T, \mu) = (111, 243)$ MeV.). The value of μ at this tricritical point is close to the values ($\mu \sim O(100)$ MeV) obtained from the analyses done by models with the local 4-Fermi interaction^{18), 20), 21), 22)} and by the SDEs with assuming the momentum dependence of the mass function.^{12), 13)} The result here implies that, in the SDE analysis, including the imaginary part moves the tricritical point to the point with smaller chemical potential; $(T, \mu) = (124, 210)$ MeV \rightarrow $(T, \mu) = (146, 20)$ MeV. Therefore we think that the imaginary part of the Dirac mass is important and should be included in the SDE at finite chemical potential.

We studied the effect of the Debye mass of gluon, and showed how the phase structure is changed. When we neglect the Debye mass, the critical temperature for the color phase transition from the 2SC phase to the QGP phase is enhanced by about 15~30%. In addition, the critical temperature T_c for the chiral phase transition from the hadron phase to the QGP phase and the critical chemical potential μ_c for the phase transition from the hadron phase to the 2SC phase are also enhanced by about 15%.

We examined the effect of antiquark contribution. Our results show that the antiquark Majorana mass gap Δ^+ is comparable to the quark one Δ^- in all the chemical potential region which we studied, $1 > \Delta^+/\Delta^- \gtrsim 0.85$ for $0 < \mu \lesssim 500$ MeV. As a

result, the approximation of neglecting the antiquark mass, which is generally considered to be good at very high density, provides quantitative differences in the phase diagram, the value of the Majorana mass gap and that of the diquark condensate.

On the other hand, the approximation of setting $\Delta^+ = \Delta^-$, which is often adopted in the analysis by models with local 4-Fermi interaction, gives almost the same results for the phase diagram, the quark Majorana mass gap and the diquark condensate as those obtained by the full analysis, in spite that the value of Δ^+ is about 15% smaller than that of Δ^- in the full analysis. Presumably, in intermediate temperature and intermediate chemical potential region it is also sufficient to set the antiquark Majorana mass equal to the quark one ($\Delta^+ = \Delta^-$) for studying other physical quantities such as the number density.

As in the previous analysis done at $T = 0$,¹⁵⁾ we sought the mixed phase, where both the chiral condensate and the diquark condensate exist, by solving the coupled SDEs for Majorana and Dirac masses with starting from several initial trial functions. However, we could not find such a solution in the present analysis.

In this paper we neglected the Landau damping of the magnetic mode of gluon since the approximated form adopted in the previous analysis¹⁵⁾ may not be valid in the low chemical potential region. It may be interesting to study the effect of Landau damping by including it as a hard thermal and/or dense loop correction without further approximation, although we may have to perform the angle integration of the SDE numerically in such a case.

We assumed that the Landau gauge provides no deviation of the wave function renormalization of the quark propagator from one even at non-zero temperature and/or non-zero chemical potential. For keeping the wave function renormalization to be one, we may have to introduce a non-local gauge fixing term as used in Ref. 27) at $T = \mu = 0$. We expect that this will not change the qualitative structure of the present results. In this paper, we have the QCD scale $\Lambda_{\text{qcd}} \sim 600$ MeV which is larger than the value determined from the experimental value of α_s in the high energy region, although the value of the pion decay constant f_π is set to be the value consistent with experiments. In Ref. 40), they use the effective coupling with including the higher order corrections to show that the values of Λ_{qcd} and f_π become consistent with experiments. It is interesting to use such a running coupling to analyse hot and/or dense QCD.

Acknowledgements

The author is very grateful to M. Harada for helpful discussions and careful reading of this manuscript.

Appendix A

— Condensates, Effective Potential and Schwinger-Dyson Equation —

In this appendix we show the explicit forms of condensates, effective potential and SDEs. The integration kernels in SDEs are different from those in Ref. 15) because the forms of the gluon propagators used in SDEs are different.

The explicit forms of the chiral condensate and the diquark condensate are given by

$$\begin{aligned}
& \langle \Omega | \bar{\psi}_a^i \psi_i^a(0) | \Omega \rangle_\Lambda \\
&= 4N_f T \sum_n \int^\Lambda \frac{d^3 p}{(2\pi)^3} \\
& \quad \left[\frac{N_c - 1}{F(p, B_1, \Delta)} \left\{ \left((p_0 - \mu)^2 - \bar{p}^2 - \{B_1(-p)\}^2 \right) B_1(p) - \Delta^+(p) \Delta^-(p) B_1(-p) \right\} \right. \\
& \quad \left. + \frac{1}{F(p, B_3, \Delta = 0)} \left((p_0 - \mu)^2 - \bar{p}^2 - \{B_3(-p)\}^2 \right) B_3(p) \right], \quad (\text{A}\cdot 1)
\end{aligned}$$

$$\begin{aligned}
& \langle \Omega | (\epsilon^{ij} \epsilon_{ab3}) [\psi^T]_i^a C \gamma_5 \psi_j^b(0) | \Omega \rangle_\Lambda \\
&= 4(N_c - 1) N_f T \sum_n \int^\Lambda \frac{d^3 p}{(2\pi)^3} \frac{1}{F(p, B_1, \Delta)} \frac{1}{2} \\
& \quad \left[\left\{ (p_0)^2 - (\bar{p} + \mu)^2 - \{\Delta^+(p)\}^2 - |B_1(p)|^2 \right\} \Delta^-(p) \right. \\
& \quad \left. + \left\{ (p_0)^2 - (\bar{p} - \mu)^2 - \{\Delta^-(p)\}^2 - |B_1(p)|^2 \right\} \Delta^+(p) \right], \quad (\text{A}\cdot 2)
\end{aligned}$$

where F is defined as

$$\begin{aligned}
F(p, B, \Delta) &= [(p_0 + \mu)^2 - \bar{p}^2 - \{B(p)\}^2] [(p_0 - \mu)^2 - \bar{p}^2 - \{B(-p)\}^2] \\
& \quad - [(p_0)^2 - (\bar{p} - \mu)^2] |\Delta^+(p)|^2 - [(p_0)^2 - (\bar{p} + \mu)^2] |\Delta^-(p)|^2 \\
& \quad + |\Delta^+(p)|^2 |\Delta^-(p)|^2 + 2B(p)B(-p)\Delta^+(p)\Delta^-(p). \quad (\text{A}\cdot 3)
\end{aligned}$$

The chiral condensate in Eq. (A.1) takes the following form when we set $\Delta = 0$ and $B_1 = B_3 = B$:

$$\begin{aligned}
& \langle \Omega | \bar{\psi}_a^i \psi_i^a(0) | \Omega \rangle_\Lambda = \langle \Omega | [\bar{\psi}_C]_a^i [\psi_C]_i^a(0) | \Omega \rangle_\Lambda \\
&= 4N_c N_f T \sum_n \int^\Lambda \frac{d^3 p}{(2\pi)^3} \frac{B(p)}{(p_0 + \mu)^2 - \bar{p}^2 - \{B(p)\}^2}, \quad (\text{A}\cdot 4)
\end{aligned}$$

where $N_c = 3$ and $N_f = 2$. The diquark condensate in Eq. (A.2) takes the following form when we set $B_1 = B_3 = 0$:

$$\begin{aligned}
& \langle \Omega | [\psi^T]_i^a C \gamma_5 \psi_j^b(0) | \Omega \rangle_\Lambda = -\langle \Omega | (\epsilon^{ij} \epsilon_{ab3}) [\psi_C^T]_i^a C \gamma_5 [\psi_C]_j^b(0) | \Omega \rangle_\Lambda \\
&= 4(N_c - 1) N_f T \sum_n \int^\Lambda \frac{d^3 p}{(2\pi)^3} \\
& \quad \frac{1}{2} \left[\frac{\Delta^-(p)}{(p_0)^2 - (\bar{p} - \mu)^2 - \{\Delta^-(p)\}^2} + \frac{\Delta^+(p)}{(p_0)^2 - (\bar{p} + \mu)^2 - \{\Delta^+(p)\}^2} \right]. \quad (\text{A}\cdot 5)
\end{aligned}$$

In this expression the first term in the square bracket is the contribution from the quark and the second term is that from the antiquark.

The explicit form of the effective potential (3.14) is given by

$$\begin{aligned}
& \bar{V}_{\text{sol}}[\Delta^+, \Delta^-, B_1, B_3] \\
& \equiv V[\Delta^+, \Delta^-, B_1, B_3] - V[0, 0, 0, 0] \\
& = -\text{T} \sum_n \int \frac{d^3 p}{(2\pi)^3} 2 \left[2 \ln \left(\frac{F(p, B_1, \Delta)}{[(p_0 + \mu)^2 - \bar{p}^2][(p_0 - \mu)^2 - \bar{p}^2]} \right) \right. \\
& \quad \left. + \ln \left(\frac{F(p, B_3, 0)}{[(p_0 + \mu)^2 - \bar{p}^2][(p_0 - \mu)^2 - \bar{p}^2]} \right) \right] \\
& - \text{T} \sum_n \int \frac{d^3 p}{(2\pi)^3} 2 \left[\frac{2}{F(p, B_1, \Delta)} \left\{ [(p_0 - \mu)^2 - \bar{p}^2 - \{B_1(-p)\}^2][(p_0 + \mu)^2 - \bar{p}^2] \right. \right. \\
& \quad \left. \left. + [(p_0 + \mu)^2 - \bar{p}^2 - \{B_1(p)\}^2][(p_0 - \mu)^2 - \bar{p}^2] \right. \right. \\
& \quad \left. \left. - [(p_0)^2 - (\bar{p} + \mu)^2] |\Delta^-|^2 - [(p_0)^2 - (\bar{p} - \mu)^2] |\Delta^+|^2 \right\} \right. \\
& \quad \left. + \frac{1}{F(p, B_3, 0)} \left\{ [(p_0 - \mu)^2 - \bar{p}^2 - \{B_3(-p)\}^2][(p_0 + \mu)^2 - \bar{p}^2] \right. \right. \\
& \quad \left. \left. + [(p_0 + \mu)^2 - \bar{p}^2 - \{B_3(p)\}^2][(p_0 - \mu)^2 - \bar{p}^2] \right\} \right. \\
& \quad \left. - 6 \right]. \tag{A.6}
\end{aligned}$$

Substituting the expression for S_{F11} into the SDEs for B_1 and B_3 in Eqs. (3.6) and (3.7), we obtain

$$\begin{aligned}
B_1(p) & = -\text{T} \sum_{n=-n_0}^{n_0-1} \int \frac{d\bar{q}\bar{q}^2}{(2\pi)^3} 2\pi\alpha_s \\
& \times K_0(q_4, p_4, \bar{q}, \bar{p}) \left[\frac{5}{6} \frac{F_+(q, B_1, \Delta)}{F(q, B_1, \Delta)} + \frac{1}{2} \frac{B_3(q)}{(iq_4 + \mu)^2 - \bar{q}^2 - \{B_3(q)\}^2} \right], \tag{A.7}
\end{aligned}$$

$$\begin{aligned}
B_3(p) & = -\text{T} \sum_{n=-n_0}^{n_0-1} \int \frac{d\bar{q}\bar{q}^2}{(2\pi)^3} 2\pi\alpha_s \\
& \times K_0(q_4, p_4, \bar{q}, \bar{p}) \left[\frac{F_+(q, B_1, \Delta)}{F(q, B_1, \Delta)} + \frac{1}{3} \frac{B_3(q)}{(iq_4 + \mu)^2 - \bar{q}^2 - \{B_3(q)\}^2} \right], \tag{A.8}
\end{aligned}$$

where

$$F_+(q, B_1, \Delta) = B_1(q)[(iq_4 - \mu)^2 - \bar{q}^2 - \{B_1(-q)\}^2] - B_1(-q)\Delta^+(q)\Delta^-(q), \tag{A.9}$$

with $q_4 = -iq_0 = (2n+1)\pi T$ and $p_4 = -ip_0$. The integration kernel K_0 is given by

$$\begin{aligned} K_0(q_4, p_4, \bar{q}, \bar{p}) &= -i \int d\Omega D_{\mu\nu}(q-p) \text{tr}(\gamma^\mu \Lambda_q^\pm \gamma^\nu) \\ &= \frac{4\pi}{\bar{q}\bar{p}} \log \frac{|\bar{q} + \bar{p}|^2 + \omega^2}{|\bar{q} - \bar{p}|^2 + \omega^2} + \frac{2\pi}{\bar{q}\bar{p}} \log \frac{|\bar{q} + \bar{p}|^2 + \omega^2 + 2M_D^2}{|\bar{q} - \bar{p}|^2 + \omega^2 + 2M_D^2}, \end{aligned} \quad (\text{A}\cdot 10)$$

where

$$\omega = |q_4 - p_4|. \quad (\text{A}\cdot 11)$$

When we set $\Delta^- = \Delta^+ = 0$, we have

$$\frac{F_+(q, B_1, \Delta = 0)}{F(q, B_1, \Delta = 0)} = \frac{B_1(q)}{(iq_4 + \mu)^2 - \bar{q}^2 - \{B_1(q)\}^2}. \quad (\text{A}\cdot 12)$$

If we further set $B_1 = B_3$, two equations in Eqs. (A·7) and (A·8) become identical. This implies that $B_1 = B_3$ is actually a solution of the SDEs for $\Delta^- = \Delta^+ = 0$.

Next, substituting the expression for S_{F12} into the SDEs for Δ^- and Δ^+ in Eqs. (3·8) and (3·9), we obtain

$$\begin{aligned} \Delta^-(p) &= T \sum_{n=-n_0}^{n_0-1} \int \frac{d\bar{q}\bar{q}^2}{(2\pi)^3} 2\pi\alpha_s \\ &\quad \times \left[K_1(q_4, p_4, \bar{q}, \bar{p}) \cdot \frac{2}{3} \cdot \frac{G_+(q, B_1, \Delta)}{F(q, B_1, \Delta)} + K_2(q_4, p_4, \bar{q}, \bar{p}) \cdot \frac{2}{3} \cdot \frac{G_-(q, B_1, \Delta)}{F(q, B_1, \Delta)} \right], \end{aligned} \quad (\text{A}\cdot 13)$$

$$\begin{aligned} \Delta^+(p) &= T \sum_{n=-n_0}^{n_0-1} \int \frac{d\bar{q}\bar{q}^2}{(2\pi)^3} 2\pi\alpha_s \\ &\quad \times \left[K_1(q_4, p_4, \bar{q}, \bar{p}) \cdot \frac{2}{3} \cdot \frac{G_-(q, B_1, \Delta)}{F(q, B_1, \Delta)} + K_2(q_4, p_4, \bar{q}, \bar{p}) \cdot \frac{2}{3} \cdot \frac{G_+(q, B_1, \Delta)}{F(q, B_1, \Delta)} \right], \end{aligned} \quad (\text{A}\cdot 14)$$

where

$$G_+(q, B_1, \Delta) = B_1(q)B_1(-q)\Delta^+(q) + [(q_4)^2 + (\bar{q} + \mu)^2 + |\Delta^+(q)|^2]\Delta^-(q), \quad (\text{A}\cdot 15)$$

$$G_-(q, B_1, \Delta) = B_1(q)B_1(-q)\Delta^-(q) + [(q_4)^2 + (\bar{q} - \mu)^2 + |\Delta^-(q)|^2]\Delta^+(q). \quad (\text{A}\cdot 16)$$

The integration kernels K_1 and K_2 are given by

$$K_1(q_4, p_4, \bar{q}, \bar{p}) = -i \int d\Omega D_{\mu\nu}(q-p) \text{tr}(\Lambda_p^\pm \gamma^\mu \Lambda_q^\mp \gamma^\nu)$$

$$\begin{aligned}
&= -\frac{\pi(\bar{q}^2 - \bar{p}^2)^2}{2\bar{q}^2\bar{p}^2\omega^2} \ln \frac{(\bar{q} + \bar{p})^2}{(\bar{q} - \bar{p})^2} + \frac{\pi}{2\bar{q}^2\bar{p}^2} \left\{ \frac{(\bar{q}^2 - \bar{p}^2)^2}{\omega^2} + 4\bar{q}\bar{p} - \omega^2 \right\} \ln \frac{(\bar{q} + \bar{p})^2 + \omega^2}{(\bar{q} - \bar{p})^2 + \omega^2} \\
&+ \frac{\pi}{2\bar{q}^2\bar{p}^2} \left[\frac{(\bar{q}^2 - \bar{p}^2)^2}{2M_D^2 + \omega^2} \ln \frac{(\bar{q} + \bar{p})^2}{(\bar{q} - \bar{p})^2} \right. \\
&\quad + \frac{\{(\bar{q} + \bar{p})^2 + 2M_D^2 + \omega^2\} \{(2M_D^2 + \omega^2)^2 + (\bar{q} - \bar{p})^2\omega^2\}}{2M_D^2(2M_D^2 + \omega^2)} \ln \frac{(\bar{q} + \bar{p})^2 + 2M_D^2 + \omega^2}{(\bar{q} - \bar{p})^2 + 2M_D^2 + \omega^2} \\
&\quad \left. - \frac{\{(\bar{q} + \bar{p})^2 + \omega^2\} \{(\bar{q} - \bar{p})^2 + \omega^2\}}{2M_D^2} \ln \frac{(\bar{q} + \bar{p})^2 + \omega^2}{(\bar{q} - \bar{p})^2 + \omega^2} \right], \tag{A.17}
\end{aligned}$$

$$\begin{aligned}
K_2(q_4, p_4, \bar{q}, \bar{p}) &= -i \int d\Omega D_{F\mu\nu}(q-p) \text{tr}(\Lambda_p^\pm \gamma^\mu \Lambda_q^\pm \gamma^\nu) \\
&= \frac{\pi(\bar{q}^2 - \bar{p}^2)^2}{2\bar{q}^2\bar{p}^2\omega^2} \ln \frac{(\bar{q} + \bar{p})^2}{(\bar{q} - \bar{p})^2} - \frac{\pi}{2\bar{q}^2\bar{p}^2} \left\{ \frac{(\bar{q}^2 - \bar{p}^2)^2}{\omega^2} - 4\bar{q}\bar{p} - \omega^2 \right\} \ln \frac{(\bar{q} + \bar{p})^2 + \omega^2}{(\bar{q} - \bar{p})^2 + \omega^2} \\
&- \frac{\pi}{2\bar{q}^2\bar{p}^2} \left[\frac{(\bar{q}^2 - \bar{p}^2)^2}{2M_D^2 + \omega^2} \ln \frac{(\bar{q} + \bar{p})^2}{(\bar{q} - \bar{p})^2} \right. \\
&\quad + \frac{\{(\bar{q} - \bar{p})^2 + 2M_D^2 + \omega^2\} \{(2M_D^2 + \omega^2)^2 + (\bar{q} + \bar{p})^2\omega^2\}}{2M_D^2(2M_D^2 + \omega^2)} \ln \frac{(\bar{q} + \bar{p})^2 + 2M_D^2 + \omega^2}{(\bar{q} - \bar{p})^2 + 2M_D^2 + \omega^2} \\
&\quad \left. - \frac{\{(\bar{q} + \bar{p})^2 + \omega^2\} \{(\bar{q} - \bar{p})^2 + \omega^2\}}{2M_D^2} \ln \frac{(\bar{q} + \bar{p})^2 + \omega^2}{(\bar{q} - \bar{p})^2 + \omega^2} \right], \tag{A.18}
\end{aligned}$$

We note that for $B_1 = 0$ we have

$$\frac{G_\pm(q, B_1 = 0, \Delta)}{F(q, B_1 = 0, \Delta)} = \frac{-\Delta^\mp(q)}{(q_4)^2 + (\bar{q} \mp \mu)^2 + |\Delta^\mp(q)|^2}. \tag{A.19}$$

Then the SDEs (A.13) and (A.14) are identical to the well-known forms given in, e.g., Ref. 8).

References

- 1) G. E. Brown and M. Rho, Phys. Rept. **363**(2002), 85, hep-ph/0103102; Phys. Rept. **269**(1996), 333, hep-ph/9504250.
F. Wilczek, hep-ph/0003183.
R. D. Pisarski, hep-ph/9503330.
- 2) S. P. Klevansky, hep-ph/9810399.
T. Hatsuda and T. Kunihiro, Phys. Rept. **247**(1994), 221, hep-ph/9401310.
- 3) K. Rajagopal and F. Wilczek, hep-ph/0011333.
- 4) K. Kanaya, hep-ph/0209116.
- 5) V. A. Miransky, *Dynamical symmetry breaking in quantum field theories* (Singapore, Singapore, World Scientific, (1993), p.533).
T. Kugo, "Basic concepts in dynamical symmetry breaking and bound state problems," KUNS-1086 *Lecture delivered at 1991 Nagoya Spring School on Dynamical Symmetry Breaking, Nakatsugawa, Japan, Apr 23-27, 1991*.
- 6) C. D. Roberts and S. M. Schmidt, Prog. Part. Nucl. Phys. **45**(2000), S1, nucl-th/0005064.
- 7) D. T. Son, Phys. Rev. D **59**(1999), 094019, hep-ph/9812287.

- 8) D. K. Hong, V. A. Miransky, I. A. Shovkovy and L. C. Wijewardhana, Phys. Rev. D **61**(2000), 056001, [ibid. D **62**(2000), 059903, Erratum], hep-ph/9906478.
T. Schäfer and F. Wilczek, Phys. Rev. D **60**(1999), 114033, hep-ph/9906512.
- 9) Y. Taniguchi and Y. Yoshida, Phys. Rev. D **55**(1997), 2283, hep-ph/9512375.
- 10) D. Blaschke, C. D. Roberts and S. M. Schmidt, Phys. Lett. B **425**(1998), 232, nucl-th/9706070.
- 11) M. Harada and A. Shibata, Phys. Rev. D **59**(1999), 014010, hep-ph/9807408.
- 12) A. Barducci, R. Casalbuoni, S. De Curtis, R. Gatto and G. Pettini, Density,” Phys. Rev. D **41**(1990), 1610.
A. Barducci, R. Casalbuoni, G. Pettini and R. Gatto, Phys. Rev. D **49**(1994), 426.
- 13) O. Kiriyama, M. Maruyama and F. Takagi, Phys. Rev. D **62**(2000), 105008, hep-ph/0001108.
- 14) O. Kiriyama, M. Maruyama and F. Takagi, Phys. Rev. D **63**(2001), 116009, hep-ph/0101110.
- 15) M. Harada and S. Takagi, Prog. Theor. Phys. **107**(2002), 561, hep-ph/0108173.
- 16) K. Rajagopal and E. Shuster, Phys. Rev. D **62**(2000), 085007, hep-ph/0004074.
- 17) R. D. Pisarski and D. H. Rischke, Phys. Rev. D **61**(2000), 051501, nucl-th/9907041.
R. D. Pisarski and D. H. Rischke, Phys. Rev. D **61**(2000), 074017, nucl-th/9910056.
- 18) J. Berges and K. Rajagopal, Nucl. Phys. B **538**(1999), 215, hep-ph/9804233.
- 19) R. Rapp, T. Schäfer, E. V. Shuryak and M. Velkovsky, Ann. of Phys. **280**(2000), 35, hep-ph/9904353.
H. Mishra and J. C. Parikh, Nucl. Phys. A **679**(2001), 597, hep-ph/0003019.
- 20) T. M. Schwarz, S. P. Klevansky and G. Papp, Phys. Rev. C **60**(1999), 055205, nucl-th/9903048.
- 21) M. Kitazawa, T. Koide, T. Kunihiro and Y. Nemoto, Phys. Rev. D **65**(2002), 091504, nucl-th/0111022; hep-ph/0207255.
- 22) B. Vanderheyden and A. D. Jackson, Phys. Rev. D **62**(2000), 094010, hep-ph/0003150.
- 23) A. Niegawa, Mod. Phys. Lett. A **17**(2002), 303, hep-th/0203045.
- 24) M. Alford, K. Rajagopal and F. Wilczek, Phys. Lett. B **422**(1998), 247, hep-ph/9711395.
R. Rapp, T. Schäfer, E. V. Shuryak and M. Velkovsky, Phys. Rev. Lett. **81**(1998), 53, hep-ph/9711396.
- 25) M. Alford, K. Rajagopal and F. Wilczek, Nucl. Phys. B **537**(1999), 443, hep-ph/9804403.
- 26) T. D. Fugleberg, hep-ph/0206033.
- 27) T. Kugo and M. G. Mitchard, Phys. Lett. B **282**(1992), 162.
- 28) M. Le Bellac, “Thermal Field Theory”(Cambridge University Press, Cambridge, England, 1996).
- 29) K. Higashijima, Phys. Rev. D **29**(1984), 1228.
V. A. Miransky, Nuovo Cim. A **90**(1985), 149.
- 30) K. Aoki, M. Bando, T. Kugo, M. G. Mitchard and H. Nakatani, Prog. Theor. Phys. **84**(1990), 683.
- 31) K. I. Aoki, T. Kugo and M. G. Mitchard, Phys. Lett. B **266**(1991), 467.
- 32) J. M. Cornwall, R. Jackiw and E. Tomboulis, Phys. Rev. D **10**(1974), 2428.
C. De Dominicis and P.C. Martin, J. Math. Phys. **5**(1964), 14, [ibid. D **5**(1964), 31].
- 33) H. Abuki, T. Hatsuda and K. Itakura, Phys. Rev. D **65**(2002), 074014, hep-ph/0109013.
- 34) J. C. Bloch, C. D. Roberts and S. M. Schmidt, Phys. Rev. C **60**(1999), 065208, nucl-th/9907086.
V. A. Miransky, I. A. Shovkovy and L. C. Wijewardhana, Phys. Lett. B **468**(1999), 270, hep-ph/9908212.
N. Evans, J. Hormuzdiar, S. D. Hsu and M. Schwetz, Nucl. Phys. B **581**(2000), 391, hep-ph/9910313.
M. Matsuzaki, Phys. Rev. D **62**(2000), 017501, hep-ph/9910541.
- 35) H. Pagels and S. Stokar, Phys. Rev. D **20**(1979), 2947.
- 36) J. Gasser and H. Leutwyler, Ann. of Phys. **158**(1984), 142.
- 37) T. Ikeda, Prog. Theor. Phys. **107**(2002), 403, hep-ph/0107105.
- 38) A. Holl, P. Maris and C. D. Roberts, Phys. Rev. C **59**(1999), 1751, nucl-th/9808076.
- 39) D. Bailin and A. Love, Phys. Rept. **107**(1984), 325.
- 40) M. Hashimoto and M. Tanabashi, hep-ph/0210115.